Fiber coupling enhancement in Optical Communication Terminals

A. Smolders

TU Delft

TNO innovation for life

Master Thesis

Fiber coupling enhancement in Optical Communication Terminals

by

A.P. Smolders

To obtain the degree of Master of Science
at the Delft University of Technology,
to be defended publicly on Wednesday November 27, 2019 at 3:00 PM.

Student number:	4217993	
Project duration:	September 24, 2018 – November 27, 2019	
Thesis committee:	M. Verhaegen	TU Delft, DCSC supervisor
	L.A. Cacace	TU Delft, Optomechatronics supervisor
	R. Saathof	TNO, Daily supervisor
	J. Spronck	TU Delft, PME
	C. Smith	DCSC

This thesis is confidential and cannot be made public until July, 2019.

Cover image credits to NASA [14]
Title: North Africa and the Mediterranean Sea
Description: An image captured from a time-lapse imagery sequence shows north Africa and the Mediterranean Sea as the International Space Station orbited 254 miles above the African continent.

An electronic version of this thesis is available at `http://repository.tudelft.nl/`.

TU Delft

Abstract

Global internet traffic is subject to exponential growth. Free Space Optical communication can accommodate for this increase. Current communication systems prove to be capable of transferring Terabits/s of data per link to and from a satellite. This is done by coupling the laser beam into a fiber, which is connected to a computer capable of processing the data in the laser beam. The downside of these systems is that they require position sensors to accurately steer the beam into the fiber. These sensors limit the amount of light reaching the receiver and thereby limit data capacity. Furthermore, these sensors may drift due to thermal loads, causing the system to lose performance.

By removing the position sensor and implementing the gradient-based algorithm Extremum Seeking Control, the same performance can be achieved without risk of fiber drift. Furthermore, this approach would reduce system complexity, relax tolerances imposed on these systems and most importantly, increase the average fiber coupling efficiency of satellite links by 40%. This is verified by a simulink model and breadboard experiment.

A. Smolders
Delft, February 2019

Contents

List of Figures

List of Tables

Glossary

AM Amplitude Modulation. 3

AO Adaptive Optics. 1, 4

BER Bit Error Rate. 4, 9

DM Deformable Mirror. 11

FSM Fast-Steering Mirror. 11

FSO Free Space Optics. 1

IoT Internet of Things. 3

OC Optical Communication. 3

OGS Optical Ground Station. 6

PAA Point-head Angle. 6

RF Radio Frequency. 3

TTS Tip-Tilt Sensor. 11

WFS Wavefront Sensor. 11

Preface & Acknowledgements

This preface serves to acknowledge that I could not have written this thesis by myself. The people who assisted me in this project deserve to be mentioned.

At TNO, I would like to thank Rudolf Saathof, for his constant availability and enthusiasm in his assistance, which extended well beyond the scope of my research. I would like to thank Andrey Khorev for his inexhaustible patience while helping me with the experimental setup. I think we had a lot of fun doing it. Kristiaan Broekens helped me with my time management by driving me to TNO at 730 in the morning, which at the very least deserves an honorary mention. I would like to thank anyone at TNO who disregarded their busy schedule to assist me in my various problems and questions. TNO is a great working environment, both due to the knowledge available and the helpfullness of its employees.

Furthermore, I wish to thank Lennino and Pieter, who I think did a great job in setting up the first Optomechatronics group at the TU Delft. Lennino's critical assessment of my project left me in constant fear whether my content was good enough, but did result in me putting in the extra effort when it was required. His technical knowledge is remarkable and I learned a lot under his tutelage.

At Systems & Control, Michel's positive attitude towards my project really sparked my own enthusiasm, which at times was questionable at best. He was a great help in steering the general course of the project.

Furthermore, I would like to thank Jo Spronck for his sporadic guidance when Lennino was not available. And again, together with Carlas Smith, for being a member of my committee.

Besides the academic part of this thesis, I had a lot of support from my family, friends and girlfriend. Without them, this thesis could not have been written.

1 Introduction

Global data transfer is subject to exponential growth. This increase can be partly accommodated for by Free Space Optical (FSO) communication links, which have the ability of sending large amounts of data between satellites and the earth. A laser beam is transmitted from an optical station, propagates through the atmosphere before arriving at an optical receiver. In this receiver the beam is coupled into a fiber, after which it is either processed by a modem or sent onward by an optical fiber connection. Current systems are capable of Terabit/s coupling by means of Adaptive Optics (AO) and sensors which accurately determine the beam focus position.

These system have their drawbacks, however. For one, the data capacity is limited by the intensity reaching the fiber. The sensors require a part of the intensity to function, which results in less light reaching the fiber. This in turn will decrease the maximum amount of data that can be sent via these links. Furthermore, the sensors that are used are not perfect and are subject to disturbance sources as noise, vibrations and thermal drift. These effects impose tight tolerances on the optomechanical design.

With this in mind, a new method of link establishment is investigated. The goal of this research is to improve fiber coupling efficiency in a Laser Communication Terminal, to accommodate for the exponential increase in global internet traffic. This will be done by applying the gradient based control algorithm Extremum Seeking Control to this problem.

The proposed fiber coupling system will be compared to an existing fiber coupler at TNO, where this research was conducted. Projects at TNO are confidential and this report will be treated as such.

The report starts in Chapter 2 by discussing the Free Space Optical (FSO) Communication and its relevance to data transfer in general. Current systems that rely on FSO Communication and in particular fiber coupling are treated in Chapter 3. The problem statement and research goal are defined here as well. Chapter 4 states the requirements for the new fiber coupling system. The optical design and the steps that led to it are shown in Chapter 5. This design is tested on its thermal and vibrational requirements in Chapter 6. Chapter 7 elaborates upon the algorithm Extremum Seeking Control and proves its stability for a Gaussian input-output mapping. Chapter 8 elaborates on the optical control parameters in the fiber coupling subsystem. Chapter 9 shows the performance of the system. Finally, Chapter 10 concludes this thesis and shows the recommendations.

2

Background

This chapter will discuss Free Space Optical (FSO) Communication and how it can accommodate for the exponential increase in global internet traffic. The advantages with respect to the more mature Radio Frequency (RF) and optical fiber technology are discussed in Section 2.1. In Section 2.2, the main challenges regarding FSO communication are presented along with current solutions to these problems. Lastly, preliminary findings are shown in Section 2.3.

2.1. The relevance of FSO communication

Free Space Optical communication is the transfer of information through the atmosphere or space rather than by means of electric wires or optical cables. Laser light close in the near-infrared spectrum is used to transfer data. The laser, like radio frequency waves, sends a series of pulses to a receiver, which are interpreted as 1's (on) and 0's (off). This is called Amplitude Modulation (AM). More sophisticated methods of communication are possible, such as (differential)-phase modulation, but this example serves the purpose of explaining data transfer.

FSO communication has a series of clear advantages with respect to the more widely used Radio Frequency (RF) communication. The main difference between optical and Radio Frequency links is the wavelength used to transmit data. Optical Communication (OC) relies on wavelengths close to the visible spectrum (1-1.5 μm), whereas the wavelength of RF links is 30 mm-3 m. The wavelength of OC links is orders of magnitude lower, which has multiple consequences. These are discussed below.

2.1.1. High data capacity

Foremost, the data rate can be up to three orders of magnitude higher than RF technology [10], playing into the desire for larger communication bandwidths. Annual global internet traffic is increasing exponentially, mainly due to Internet of Things (IoT), which is the connection of population and devices to the internet and each other. Autonomous vehicles are an important part of the internet traffic increase [4]. RF technology will soon reach its ceiling in terms of data rates, but FSO is able to accommodate for this increase [22].

2.1.2. Narrow beam divergence

Optical Communication links have a far lower beam divergence. An optical link diverges to a far field diameter of roughly a 100 m when it connects to a GEO-satellite, whereas RF links spread out to multiple kilometers (See Figure 2.1).

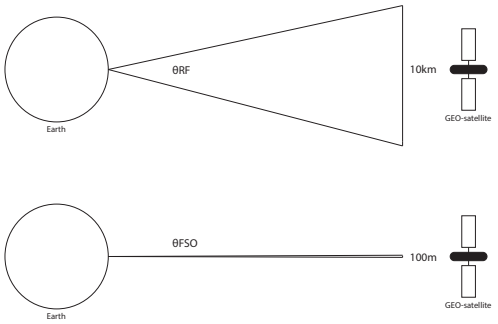

Figure 2.1: Divergence of Radio Frequency (top) and Optical (bottom) links

Low beam divergence results in OC links being more secure. It also eliminates the need for spectrum licensing, as different beams do not interfere with each other. Most importantly, the narrow beam divergence results in an increase in intensity arriving at the receiver. This in turn results in smaller, lower weight components which make satellites more cost-effective. Table 2.1 compares antenna length and mass of optical and RF communication systems. An equal data rate of 2.5 Gbit/s is assumed for both systems.

Table 2.1: Comparison of antenna length and mass for Geostationary Earth Orbit (GEO) and Low Earth Orbit (LEO) links using optical and RF communication systems. Values in parentheses are normalized to the optical parameters. [18]

Link	Optical	RF
GEO-LEO		
Antenna Diameter	10.2 cm (1.0)	2.2 m (21.6)
Mass	65.3 kg (1.0)	152.8 kg (2.3)
GEO-GEO		
Antenna Diameter	13.5 cm (1.0)	2.1 m (15.6)
Mass	86.4 kg (1.0)	145.8 kg (1.7)
LEO-LEO		
Antenna Diameter	3.6 cm (1.0)	0.8 m (22.2)
Mass	23.0 kg (1.0)	55.6 kg (2.4)

2.1.3. Feasibility for link establishment in remote areas

Optical fibers rely on the same frequency as FSO communication and can achieve the same data rates. They are a reliable alternative to FSO communication and are already widely in use [2]. However, for the greater part of earth's surface, optical fibers are both physically and financially impractical [9]. Additionally, a major factor of internet traffic increase is related to vehicles which cannot connect to optical cables. Optical communication satellites are a good alternative to provide connectivity in these cases.

2.2. Challenges and mitigations in FSO communication

Despite the great potential of FSO communication, there are some challenges that arise due to the lower wavelength of the carrier. The main ones are discussed below, as well as the techniques current systems have to mitigate these challenges.

2.2.1. Atmospheric effects

Atmospheric turbulence

The lower wavelength of light used in FSO results in more interaction with the atmosphere. Since the speed of light is dependent of the density of the atmosphere and the atmospheric density is not constant along the optical beam, parts of the beam will arrive at the satellite at different moments in time. Eventually, this results in a higher Bit Error Rate (BER), which is a 1 being incorrectly interpreted as a zero or vice versa at the receiver. As this is not desirable, the system needs to correct for it. This is done by means of Adaptive Optics (AO). Figure 2.2 shows how this is done.

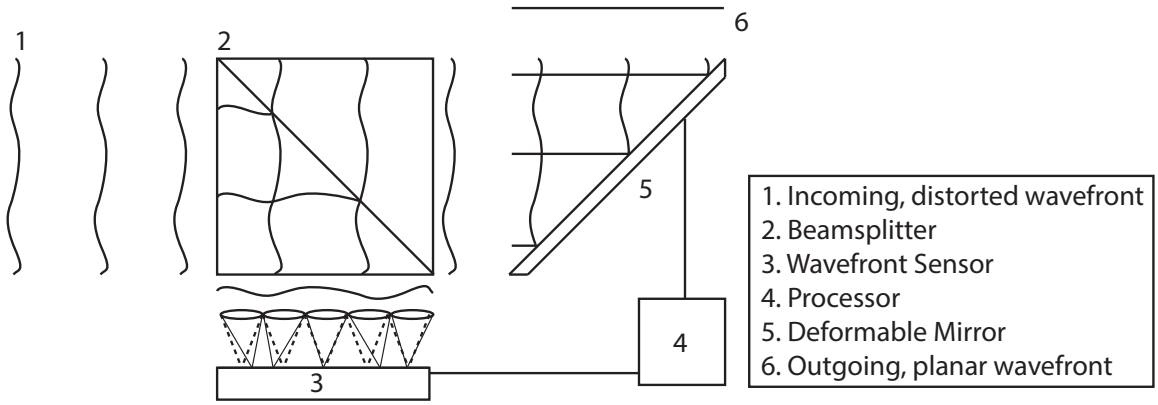

Figure 2.2: Wavefront correction

A distored wavefront (1) arrives at an optical receiver. This light is partly channeled by a beamsplitter (2) to a Wavefront Sensor (3). This sensor is able to measure the profile of the wavefront. Knowing the distortion, a processor (4) calculates how a mirror (5) should be deformed, such that the outgoing wavefront (6) is perfectly flat again. This mirror is called a Deformable Mirror (DM) and consists of a series of small actuators which can locally change the surface of the mirror.

Attenuation
As light travels through the atmosphere it loses intensity due to absorption and scattering. In the RF transmission window, this intensity loss is negligible. At frequencies near the visible spectrum, however, attenuation is much higher and poses a problem in data transfer. Figure 2.3 shows the transmittance as a function of wavelength when light propagates through a kilometer of atmosphere. It can be seen that lower wavelengths generally result in a lower transmittance. This is a result of scattering, which becomes larger as the wavelength decreases. Additionally, specific wavelength are absorbed by molecules in the air such as H_2O, CO_2 and O_3. Transmittance at these frequencies is low and should be avoided.

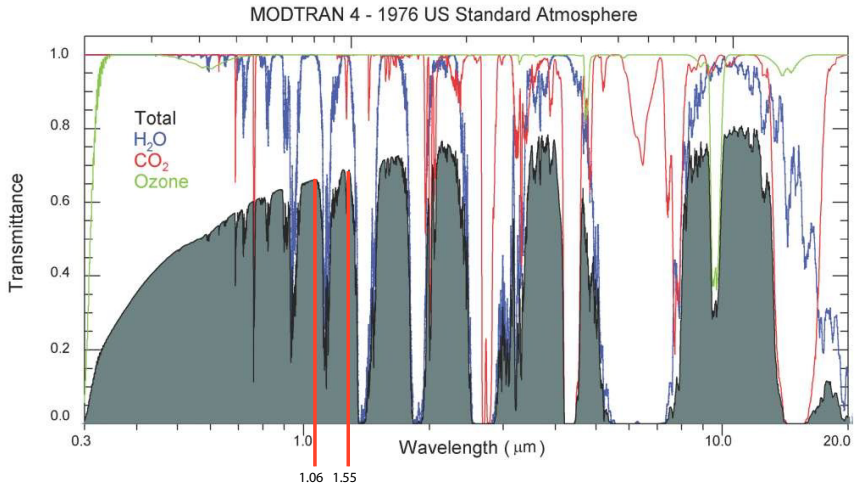

Figure 2.3: Atmospheric transmittance over wavelength. 1.06 μm and 1.55 μm correspond to transmission peaks [15]

There are two peaks around 1.06 μm and 1.55 μm which allow high transmittance. These are the two mainly used carrier frequencies today. For clear weather conditions and a 1.55 μm carrier wavelength, the transmittance is approximately 70% after a kilometer of propagation in high-density atmospheric regions [11]. In optical fiber communication, attenuation is also wavelength dependent. Figure 2.4 shows experimental data in fiber attenuation, with a minimum around 1.55 μm.

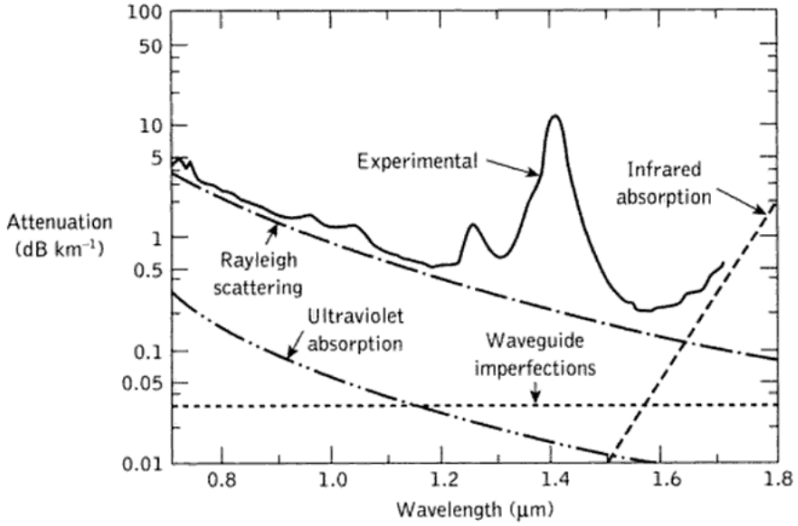

Figure 2.4: Fiber attenuation over wavelength [1].

Note that low attenuation means high transmittance. The experimental line shows the fiber attenuation, which is to be as low as possible. Appropriate choice of carrier frequency will result in the lowest possible attenuation in the near-infrared transmission window. As most FSO communication systems are combined with fiber optics, a wavelength of 1.55 μm is the proper choice. It has high transmission in both free space and fibers and still has the potential of achieving Terabit/s data rates [17].

2.2.2. Weather conditions

Weather conditions form their own challenges in link establishment. In heavy fog or cloudy environments, attenuation in the optical channel can be as much as 350 dB/km, rendering link establishment impossible [13]. This can be solved by a technique called site diversity. In practically all cases the signal can be relayed to another ground or space station which path is cloud-free [6].

2.2.3. Pointing accuracy

Table 2.2 shows speeds and altitudes of LEO and GEO satellites. In RF communication, the large divergence of the transmitting beam makes it easy to reach the satellites even at these speeds and altitudes. As the beam divergence of the FSO link is approximately three orders of magnitude lower than the RF link, it will become more difficult to establish a link between an Optical Ground Station (OGS) and satellite.

Table 2.2: Altitude and speeds of satellites

Satellite	**LEO**	**GEO**
Altitude	200-2,000 km	35,786 km
Speed	6.9–7.8 km/s	3.1 km/s

Usually, this is solved by receiving a RF signal from the satellite. The high divergence of the Radio Frequency beam will ensure the Optical Ground Station will be reached. With position sensors, it is possible to determine at which angle the RF beam enters the OGS. With this angle the position of the satellite can be determined. The movement of the satellite has to be taken into account as well. When the OGS transmits a signal to the satellite, it will point ahead of the satellite in order to reach it at the right place. As the speed of the satellite is known, the Point-Ahead Angle (PAA) can be calculated. The process of link establishment is called Pointing, Acquisition and Tracking (PAT). Current communication systems are capable of establishing optical links, despite the high pointing accuracy requirements [8].

2.3. Preliminary findings

Free Space Optical communication has a three orders of magnitude higher data capacity compared to Radio Frequency technology. The beam divergence is lower, which relaxes the requirements on input power. It also results in lower weight components which make systems more cost-effective. FSO communication is more secure, its spectrum is unlicensed and can be used where optical fibers cannot be used.

Atmospheric effects and weather conditions deteriorate performance of FSO communication if not accounted for. Link establishment is also more difficult due to the narrow beam divergence of optical links. However, an appropriate choice of carrier wavelength and the use of Adaptive Optics and Pointing, Acquisition and Tracking algorithms prove to be effective against these challenges. Thus, establishing FSO links is technically feasible and proves to be an excellent solution to the global internet traffic problem.

3

Literature research: Current fiber coupling systems

This chapter will discuss optical communication links in use. Section 3.1 states the importance of fiber coupling in optical links. Section 3.2 shows how current systems achieve link establishment. The drawbacks of current systems are presented in Section 3.3. The research goal is defined in Section 3.4.

3.1. Fiber coupling in optical communication

Figure 3.1 shows how an optical communication terminal would be used. The ground station (1) establishes an optical link with a satellite (2). The satellite connects to the user (3) via RF links. The satellite could also send an optical signal to another satellite before connecting back to the earth. The objective of the optical communication link is to maximize data rates while keeping the bit error rate (BER) at a minimum. The bit error rate is the amount of wrongly interpreted bits in a signal. As the BER grows higher, signal quality diminishes. It is desirable to keep the Bit Error Rate below 10^{-6} for any communication link [1].

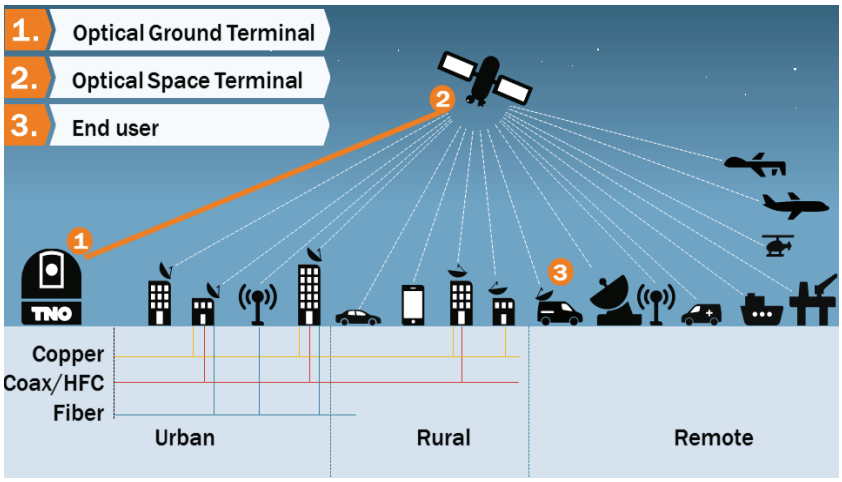

Figure 3.1: Optical communication architecture [17]

Usually, the beam entering a satellite is coupled into a fiber, which is connected to a modem capable of processing the data and sending it onward. Free space detectors are also in use, which are detectors that process data from an optical beam without the need of fiber coupling. The majority of current systems rely on optical fibers, however [16]. The main advantage of fiber optics is the high reliability with which it can send data onward due to optical fiber amplifiers. Fiber coupling efficiency is an important factor in reaching high data rates with a low BER. If the fiber coupling fails, the entire system will fail. It is therefore sensible to look at fiber coupling efficiency and how it can be optimized.

3.1.1. The principle of fiber coupling

Figure 3.2 shows the basic principle of fiber coupling. Optical fibers consists of a core in which the light is guided, surrounded by a cladding which ensures no light is refracted. This is accomplished by choosing the index of refraction of the core (n_1) slightly higher than that of the cladding (n_2). This ensures total internal reflection for incident light angles higher than the critical angle θ_c (see Figure 3.2). Incident angles below θ_c are partly refracted and are therefore not guided. The critical angle directly depends on $\Delta n = n_1 - n_2$ and limits the Numerical Aperture (NA) of the fiber. The NA is the sine of the maximum angle (α) that is still guided through the fiber.

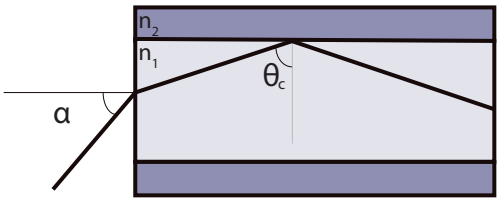

Figure 3.2: Visualisation of Numerical Aperture

3.1.2. Calculating fiber coupling efficiency

Fiber coupling efficiency is the amount of light coupled into the fiber over the amount of light reaching the fiber. If there is less light reaching the fiber, the efficiency can remain the same, but overall fiber coupling decreases. Fiber coupling efficiency can be calculated by determining the overlap between the spot focus and fiber core. More specifically, it is the overlap integral of the electric field distributions of spot and fiber and can be calculated by Equation (3.1) [21].

$$\mathrm{OI} = \frac{\left|\int\int E_1(x,y)\cdot E_2(x,y)\,dx\,dy\right|^2}{\left|\int\int E_1(x,y)\right|^2 dx\,dy \cdot \left|\int\int E_2(x,y)\right|^2 dx\,dy} \tag{3.1}$$

Here, E_1 is the electric field distribution of the spot focus, E_2 is the distribution of the fiber. The incoming beam is assumed to be a planar wavefront with finite width d. The focusing of such a beam will result in an electric field distribution as depicted in Figure 3.3 and intensity distribution as depicted in Figure 3.4.

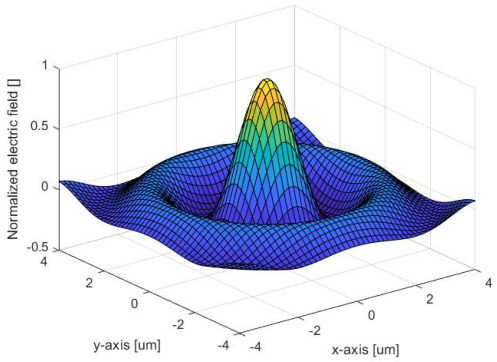

Figure 3.3: Electric field distribution of spot focus

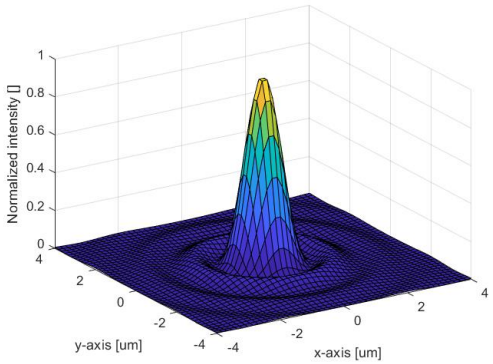

Figure 3.4: Intensity distribution of spot focus

These distributions correspond to the Airy disk pattern. The size of this airy disk is determined by the focal length of the lens, beam diameter and wavelength of the light. The electric field that is guided through the fiber is a Gaussian distribution determined by the mode field diameter w_c of the fiber. This is a characteristic of a fiber and typically ranges from 3-12 µm. The focal length and beam diameter must be chosen that these distributions are matched as closely as possible.

3.2. Functioning of current Optical Communication Terminals

Here, a current optical communication systems that entails fiber coupling is shown.

3.2.1. Current fiber coupler: breadboard design

TNO has a variety of projects which focus on high-bandwidth laser communication. These projects involve Optical Ground Stations which use an active fiber coupling system [5, 16]. Figure 3.5 shows OFELIA, an optical communication terminal used in testing for atmospheric disturbances. Figure 3.6 shows a schematic representation.

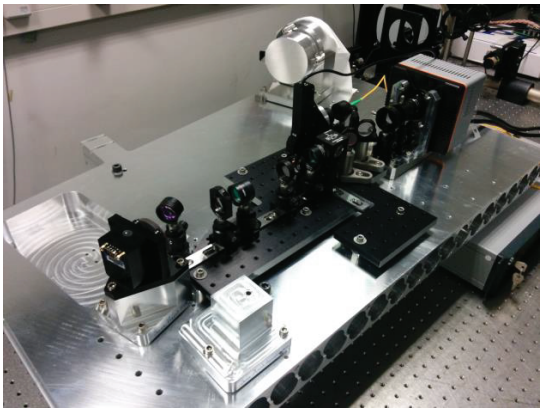

Figure 3.5: OFELIA breadboard [17]

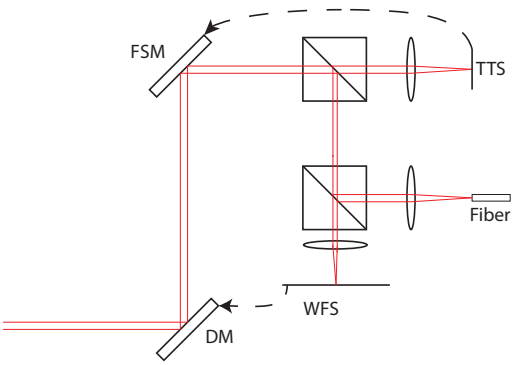

Figure 3.6: Schematic representation of OFELIA

Figure 3.7: Schematic representation of OFELIA, with several beamsplitters (BS), a wavefront sensor (WFS), tip-tilt sensor (TTS), a fast steering mirror (FSM) and deformable mirror (DM)

Light enters the system on the left and hits the Deformable Mirror (DM) and Fast Steering Mirror (FSM). Two beamsplitters channel part of the light to a Tip-Tilt Sensor (TTS) and Wavefront Sensor (WFS). As tip-tilt is the major disturbance in the atmosphere, wavefront correction is usually split up in tip-tilt correction and higher-order wavefront correction. Drift, vibrations and atmospheric turbulence can all displace the spot focus with respect to the fiber center. If this happens, the TTS can measure this deviation and the FSM can correct for it by changing its angle with respect to the beam. The wavefront sensor is able to measure higher order aberrations, which the DM can correct for in the same way.

3.3. Problem statement

There are various disturbances that impede performance of communication links. The most important ones are atmospheric turbulence, satellite (and ground) vibrations and thermal drift. To mitigate these disturbances, optical terminals use position sensors and wavefront sensors. Higher order aberrations are handled by the wavefront sensor, while the position sensor negates atmospheric tip-tilt, vibrations and thermal drift. These systems have proven to be effective in high-capacity link establishment with low aberrations. In ensuring this high capacity and reliability, current systems have a few accompanying downsides. They are discussed below.

3.3.1. Intensity loss

The first downside of the WFS and TTS is that they require a part of the beam intensity to function. This means the intensity reaching the fiber is only a fraction of the light arriving at the optical station. This directly results in lower fiber coupling. In the LEOCAT-project of TNO, a beamsplitter channels 35% of light intensity towards the position sensor [20].

3.3.2. Relative motion between sensor and fiber

The tip-tilt sensor is capable of correcting for drift, vibrations and atmopsheric tip-tilt. However, the sensor itself might be subject to drift and vibrations. If the sensor moves with respect to the fiber due to temperature fluctuations, any correction due to the TTS can actually deteriorate performance. The spot will be controlled to the position which the TTS considers optimal, but this no longer coincides with optimal fiber coupling.

The same goes for vibrations which are not equal for TTS and fiber, which are mainly due to eigenmodes in the subsystem. Of course, thermal stability is taken into account in the design process and a proper optical design will not suffer from these limitations as much. That does mean that tight tolerances have to be taken into consideration, which limit your design space and complicate fabrication. In LEOCAT, performance loss due to fiber movement is 13.7% [20].

3.4. Research goal

The objective in an optical link establishment is to achieve an as high as possible bandwidth, with an as low as possible Bit Error Rate (BER). As the BER increases with a diminishing incoming intensity, the latter is to be maximized. Fiber coupling is denoted as the amount of light coupled into the fiber. The objective is to maximize this, either by diminishing factors that contribute to coupling losses, or by increasing the amount of light reaching the fiber. This leads to the following research goal:

The goal of this research is to improve fiber coupling efficiency in a Laser Communication Terminal, to accommodate for the exponential increase in global internet traffic.

4

Requirements and proposed concept

This chapter will discuss the requirements imposed on the fiber coupling system. These requirements form the basis for the design choices that will be made. The requirements are largely derived from a similar fiber coupling system in LEOCAT, with which the new design will be compared. Henceforth, the new design will be called proposed design or proposed concept.

Section 4.1 shows the user requirements and error budget for the proposed design. The optical and mechanical requirements that are derived from this are discussed in Section 4.2. Section 4.3 explains the environment in which the system is operating in. The control algorithm requirements are shown in Section 4.4. **??** explains the proposed concept and Section 4.6 concludes this chapter.

4.1. User requirements and error budget

The requirements that the new design is imposed to are based on requirements of a current optical system within TNO. The two systems are compared, such that the new system's performance can be quantified. The user requirements are shown in Table 4.1.

Table 4.1: User requirements for fiber coupling subsystem

Property	**Requirement**
Fiber coupling efficiency	0.35
Wavelength	1550 nm
Mode field diameter of fiber	10.4 μm
Entrance aperture	10 mm

A higher efficiency is considered better as it diminishes the Bit Error Rate. As discussed, the laser communication system uses a wavelength of 1550 nm. The entrance aperture of the fiber coupler, which is the diameter of the beam hitting the FSM, is 10 mm. These user requirements result in optical and mechanical system requirements. Besides these requirements, a few aims are kept in mind. The subsystem needs to be operational in space. As increasing the weight will increase the cost of sending the satellite to space, the design is to be as low-weight as possible. This leads to a preference of using low-weight materials and a designing the system to be as compact as possible.

The efficiency shown in Table 4.1 comes from an error budgetting, which shows efficiency losses due to various factors. Table 4.2 shows the error budgeting of the current system (left) and proposed system (right). Note that the composition of the coupling budget was an iterative process. The motivation for certain values will be given in subsequent chapters.

Table 4.2: Coupling loss budget [20]

Contributor	Tolerance current	RCE current	Tolerance new	RCE new
Light going to quadcel		0.65		-
Theoretical efficiency		0.817		0.817
Fresnell losses		0.96		0.96
Fiber decenter	2 μm (stability + alignment)	0.863		-
Fiber tip/tilt	1.41°	0.946	1.41°	0.946
Fiber defocus	20 μm	0.984	20 μm	0.984
WFE	100 nm RMS	0.837		0.837
Atmospheric tip/tilt		-		0.96
Satellite microvibrations		-		0.59
Dithering amplitude a		-	0.5 μm	0.98
Total		0.350		0.352
Requirement		0.35		0.35

Here, RCE stand for the remainder of coupling efficiency in percents. In the current design, 35% of the light entering the subsystem is channeled to the position sensor. Next, there is a maximum theoretical efficiency when a flat wavefront is coupled into the fiber, which holds for both designs. Fresnel losses are due to the light partly reflecting from the fiber and occur in both situations. Next, due to misalignment of the fiber in manufacturing, the system can lose efficiency. These are divided in decenter, tip/tilt and defocus. These misalignments impose mechanical requirements of the system, which are discussed in Section 5.3. In the current system, decenter is the most critical tolerance, as a 2 μm deviation already results in a 14% efficiency loss. The proposed system is not impacted by this, as decenter is corrected for in real-time by a control algorithm. Next, the higher order aberrations are expected to amount to an efficiency loss of 16%. This is due to imperfect wavefront correction with the DM, and occurs in both systems. Then there are a few factors that are not impacting the current system, but do result in an efficiency loss in the proposed system. These are atmospheric tip/tilt and satellite microvibrations. The current system is very fast in correcting these errors, due to the position sensor. Therefore, no loss of performance is expected due to these contributors. The proposed system is not as fast, however, and not all vibrations and tip/tilt can be corrected for. Furthermore, the proposed system finds the optimum by circelling around its current position with dithering amplitude a, which also results in performance loss.

The largest difference between the two systems is that the proposed design does not use a position sensor. How fiber coupling can still be achieved without the position sensor will be explained in Section 4.5. The error budget imposes optical, mechanical and control requirements on the system. These are explained in Section 4.2 to Section 4.4. The subsequent chapters show whether these requirements can be met.

4.2. Optical and mechanical system requirements

Firstly, the user requirements results in optical requirements. They are shown in Table 4.5.

Table 4.3: Optical requirements for fiber coupling subsystem

Property	Requirement	Remarks
Spot size	9.2 μm	-
f	46.7	The focal length that achieves the spot size of 9.2 μm
Manufacturing tolerances	50 μm	The components of the fiber coupling system must be positioned within a 50 μm range, to ensure
Alignment plan z-axis	-	To ensure a maximum fiber defocus of 20 μm, an alignment plan will be needed.

As there is a maximum efficiency when coupling a flat wavefront into an optical fiber, a specific spot size must be chosen. In the case of a fiber with a mode field diameter of 10.4 μm, the spot focus must be 9.2 μm. Now, as the beam diameter is known, the focal length to achieve this spot size can be calculated. The ratio between the focal length and beam diameter determines the spot size. Figure 4.1 shows various ratios that result in a

different efficiency. It shows a maximum at f/D at 4.6719, so the focal length must be 46.6719 mm. Note that this maximum efficiency corresponds to the 81.7% found in literature.

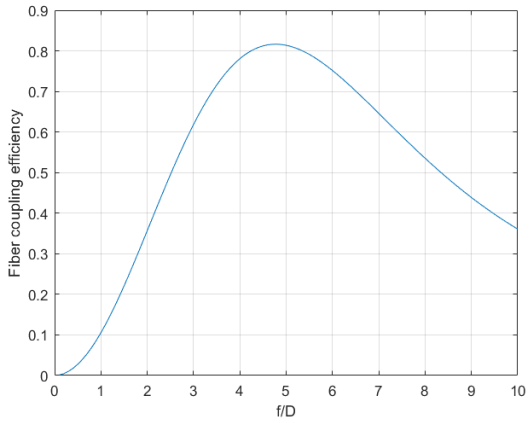

Figure 4.1: Fiber coupling efficiency as a function of f/D. Theoretical maximum at f/D ≈ 4.6719 for mode field diameter of 10.5 μm

4.3. Operational environment

Other than meeting it's efficiency requirement, the system must be operational in space. Satellites are subject to varying temperatures during operation, called a thermal cycle. Furthermore, there are micro-vibrations in the satellite due to moving parts. The system must also survive the launch, where it is subject to large amplitude vibrations. All relevant environmental conditions are discussed in Table 4.4.

Table 4.4: Operational environment for fiber coupling subsystem

Environment	Requirement	Remarks
PSD of launch vibrations	Survive	Characteristics shown in Figure 4.2
Temperature drop of -70 °	Survive	-
Thermal cycle	Meet performance requirement	-
Satellite vibrations	Meet performance requirement	Characteristics shown in Figure 4.3a
Atmospheric turbulence	Meet performance requirement	Characteristics shown in Figure 4.3b
Vacuum environment	Meet performance requirement	-

The satellite must be operational in a vacuum environment. This impacts material choice in the design, as some materials will evaporate due to the low pressure. The characteristics of the other environments will discussed below.

4.3.1. Satellite launch conditions

The launch of a satellite is a serious constraint on the optical design of an Optical Space Station. It is subject to large vibrations, of which the characteristics are shown in Figure 4.2. Furthermore, the satellite will experience a temperature drop of up to 70 degrees. The satellite must survive this, which means it must not show signs of material failure or plastic deformation.

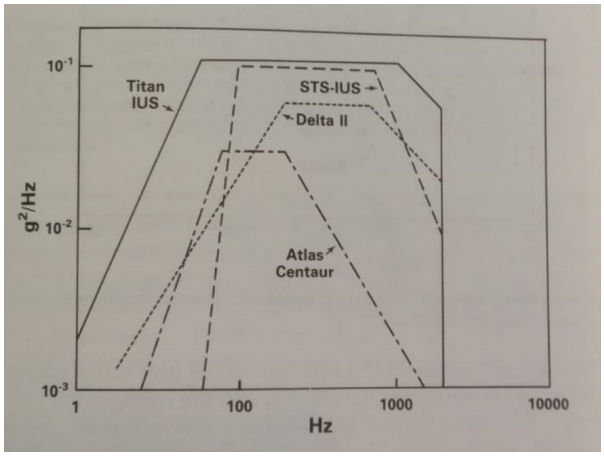

Figure 4.2: PSD of satellite launch vibrations [3]

4.3.2. Environmental conditions during operation

During operation, the satellite must meet the performance requirements discussed in Table 4.1. Most important factors are temperature fluctuations, extremely low pressure and internal vibration sources of the satellite. The satellite will heat up and cool down, depending on its orientation and position with respect to the sun and earth. This is called a thermal cycle, and it is assumed to range from -20 °C to 40 °C. The microvibrations the satellite is subject to are shown in Figure 4.3a. The characteristics of atmospheric tip/tilt the beam is subject to is shown in Figure 4.3b.

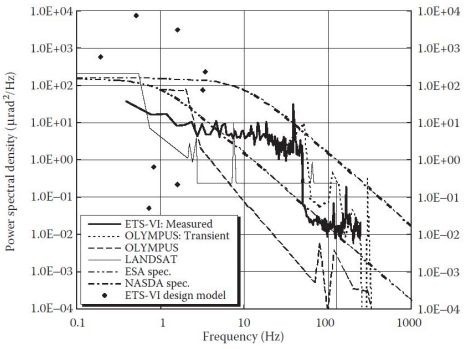

(a) PSD of satellite microvibrations [19]

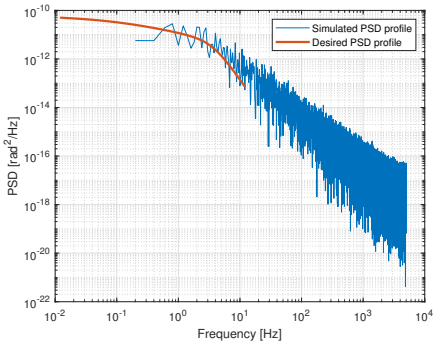

(b) PSD of atmospheric turbulence

For microvibrations, the ESA-spec (.–) line will be chosen as it is a common specification within TNO. The largest part of these signals are low-frequency content. When the system needs to survive, it means that no plastic deformation must occur, or material failure such as lens cracking. When the system is operational, the coupling loss due to the atmosphere and satellite vibrations must not exceed the values specified in Table 4.2.

4.4. Control system requirements

As the system needs to maintain an efficiency of 0.35, the disturbances shown in Figure 4.3a and Figure 4.3b must be rejected up to a certain degree. This puts a requirement on the control bandwidth. The proposed system acts as a low pass filter in terms of disturbance rejection, where lower frequency disturbances are rejected better. The higher this corner frequency is, the better the disturbance rejection. Furthermore, the amplitude of dithering results in a coupling loss, due to the spot circling around the optimum.

Table 4.5: System requirements for fiber coupling subsystem

Property	Requirement	Remarks
Minimum dithering frequency	250 Hz	A higher control bandwidth is better, as it leads to a higher suppression of disturbances.
Maximum dithering amplitude	1 μm	A lower dithering amplitude is better, as the spot stays closer to the optimum. Eventually, this is limited by the amount of noise and disturbances of the system.

4.5. Proposed concept

4.5.1. Concept of sensorless fiber coupling

As could be seen in Table 4.2, a large portion of the light is lost to the position sensor. Secondly, a large tolerance in decenter has to be taken into account, which also decreases efficiency by 14%. Both contributors are due to the position sensor. Therefore, in the proposed design the position sensor is removed entirely. From here on out, this design will be called 'sensorless fiber coupling', rather than 'position sensorless fiber coupling', for simplification. The optimal spot position will be found using intensity measurements of the fiber. Tip-tilt, vibrations and drift will all result in a decrease in incoming intensity. This can be measured by the on-board computer and corrected for by the FSM. The fiber is already connected to a modem capable of processing the data stream, which means intensity measurements are readily available. Figure 4.4 shows the proposed fiber coupling subsystem.

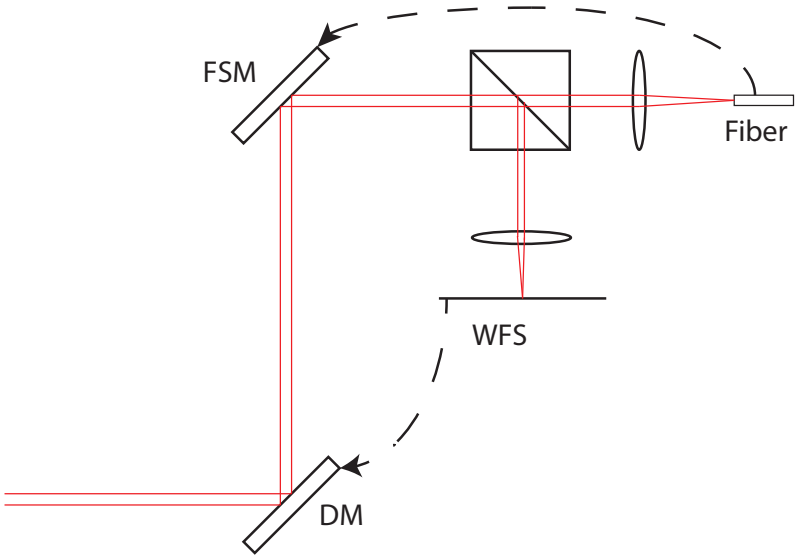

Figure 4.4: Schematic representation of fiber coupling without TTS

As can be seen, the position sensor is removed from the system and intensity data from the fiber is used to adjust the FSM. In this figure, the striped arrow signifies a feedback signal. If this setup is feasible, the two main drawbacks of fiber coupling in an optical link are mitigated. There is no loss of intensity to the sensor, and sensor drift and vibrations are no longer an issue. Additionally, it reduces system complexity as it removes a beamsplitter and a sensor. It also relaxes the requirements on the optical design, as the fiber position is no longer essential in functioning of the system. It does not matter where the fiber exactly is, as long as the FSM can still find the optimum. That means thermal drift is no longer an issue, given that the algorithm is faster than the drift rate.

4.5.2. Sensorless fiber coupling control: Input-output mapping

Optimizing the position of this beam is the principle control problem. In sensorless fiber coupling, only measurements of current fiber coupling efficiency are available. A static mapping from position (input) to

this intensity (output) is given in Figure 4.5.

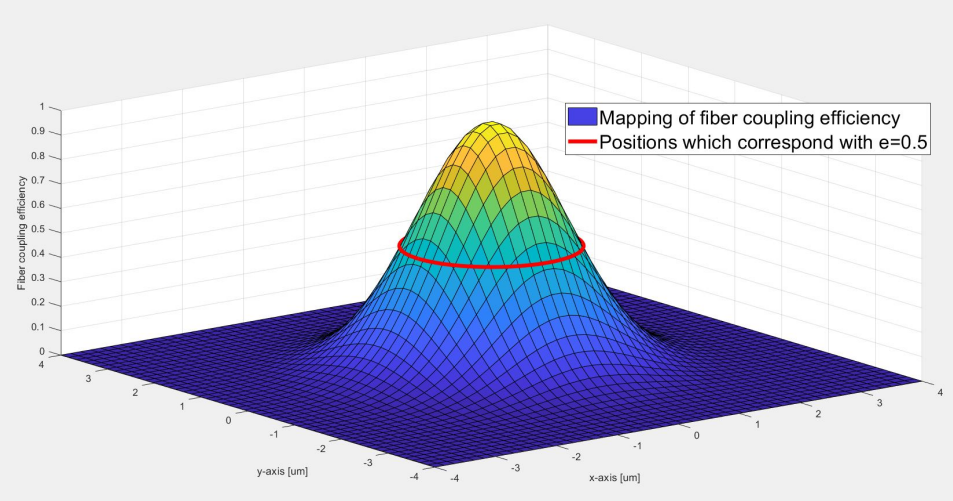

Figure 4.5: Efficiency over spot position. The red ring indicates multiple positions with equal efficiency

There are a couple of things that can be observed from this illustration. First, the mapping has a maximum in the center, when the fiber center and spot center are perfectly aligned. Secondly, it can be seen there are multiple spot positions corresponding to the same efficiency. In fact, every intensity corresponds to a ring of possible positions. The positions corresponding to an efficiency of 0.5 are highlighted in Figure 4.5 to illustrate this. This means there is no 1-to-1 mapping, which complicates the control problem. After all, a single intensity measurements does not give enough information to know the direction of optimal movement.

It is known that the fiber coupling problem is not static, as both the fiber and the spot position can move over time. Also, fiber orientation and wavefront errors will change the shape and size of this mapping.

4.5.3. Gradient estimation

A method must be devised to find the direction to the optimum. As only intensity measurements are available, a logical solution would be to look at consecutive measurements in intensity. As the spot moves around, the intensity will likely increase or decrease with it. Consecutive output measurements constitute a gradient, which can directly be used to determine the desired direction of movement. Gradient estimation needs to be performed under the disturbances including vibrations, noise and atmospheric turbulence. Furthermore, the optimal position needs to be found in both x- and y-axis.

A promising approach in gradient estimation is called Extremum Seeking Control (ESC). Since the proof of stability for a general nonlinear dynamic map, this algorithm has risen in popularity considerably [12]. It is shown ESC can be applied in general optical systems with self-tuning components [7]. The great advantage of ESC over other gradient estimators is its resistance to noisy environments. It imposes a sinusoidal perturbation at a specific, known frequency to the system. As only this frequency content is of importance, other frequencies can be filtered out. The perturbation frequency can be chosen such that the disturbances have minimal effect on system performance. Furthermore, a decoupling of x and y-axis can be achieved by applying a 90° phase shift between the two perturbation directions. Extremum Seeking Control will be explained in more detail in Chapter 7.

4.6. Conclusion

The requirements for the system have been set up, and an error budget has been made. It has been chosen to remove the position-sensor in the fiber coupler, for numerous reasons. It increases incoming intensity in the fiber and relaxes tolerances on the fiber position. Furthermore, the removal of a beamsplitter and sensor makes the system smaller and more light-weight. The optimal spot position can still be found by relying on intensity measurements in the fiber (rather than position measurements for a separate sensor). This can be done by the gradient-based control algorithm Extremum Seeking Control.

5

Optical design

5.1. Introduction

This chapter gives an overview of the optical design and the steps that led to it. This system consists of an FSM, a focusing element and a fiber. These components need to be mounted within certain tolerances, and must remain stable under thermal and vibrational conditions. Section 5.2 shows different concepts, where the most promising one is chosen. Section 5.3 elaborates on a tolerance analysis of this design. Section 5.4 discusses the alignment and manufacturing of the design. Section 5.5 concludes this chapter.

5.2. Concept generation

The incoming collimated light needs to be coupled into the fiber, which means it must be focused. This can be done by either a lens or a mirror. Three concepts will be compared. They are shown in Figure 5.2.

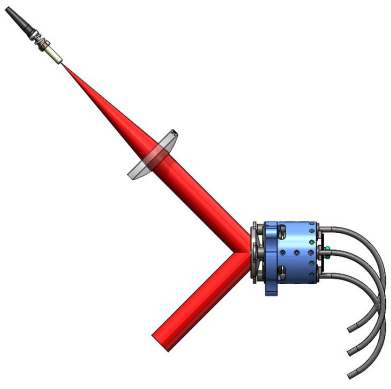

Concept A: Lens as converging element

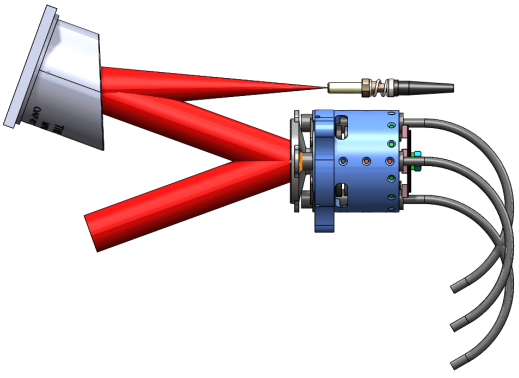

Concept B: Mirror as converging element

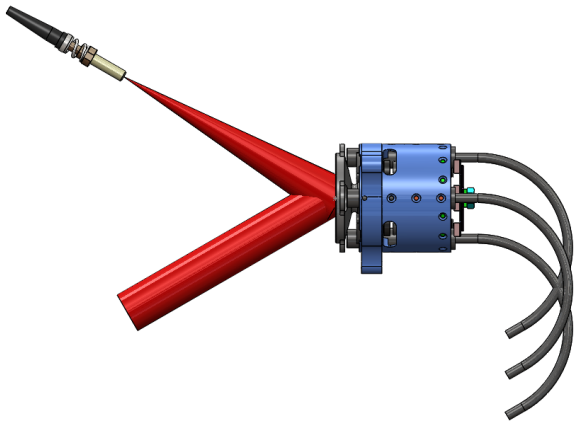

Figure 5.2: Concept C: FSM as converging element

Concept A uses a lens as a converging element, concept B and C make use of a mirror. Note that the FSM is the same size in all concepts. Concept C alters the FSM such that the mirror surface ensures the beam converges to the fiber. While optically the same, there are some differences between reflective and refractive optical elements. The impact these differences will have on requirements is discussed below. Table 5.1 shows how well the concepts score and results in a choice of concept.

Table 5.1: Considerations for optical converging element

Concept characteristic	**A**	**B**	**C**
Volume	-	+	++
Robustness	-	+	+
Thermal robustness	-/0	+	+
Optical performance	+	0	- -
Cost	+	0	0
Availability	+	+	- -

- **Volume**: Due to optical beam folding, the concepts that use a mirror are able to make the system more compact. Concept C has one component less. Furthermore, the incoming angle can be a lot smaller, making the system even more compact.
- **Robustness**: Metals are ductile, while lenses are brittle. The concept must survive the launch, so concepts that use an aluminium mirror are more suitable for space applications.
- **Thermal robustness**: Lenses need to be mounted to other materials, which have different thermal expansion coefficients. Relative expansion will lead to stresses in the lens. This leads to a risk of lens cracking. The mirror concepts can be fully homogeneous in terms of material and do not have local thermal deformations. The entire system expands homogeneously and there will be no stresses imposed on the mirror.
- **Optical performance**: An angular misalignment will result in twice the tip/tilt when a mirror is used, compared to a lens. However, the FSM will be able to correct for angular misalignment. Misalignment in the optical axis will be the same for both elements. Any surface roughness will results in twice the aberration in case of the mirror when it reflects. This means tighter tolerances must be imposed on surface roughness when manufacturing. This is out of the scope of this research, however, and it is assumed both optical elements can be manufactured within spec. Two things need to be said about concept C. First, the axis of rotation of the FSM that is available is not on the optical surface. That means that a tip/tilt will also result in a decenter of the mirror. Now, for a flat mirror this does not influence optical performance. Decenter in a curved mirror, however, results in a decenter of the spot. This means that correcting with tip/tilt introduces additional decenter in the system. This will make it harder to achieve a reliable dithering amplitude. Therefore, when designing a parabolic mirror on the FSM, the axis of rotation must be on the optical surface, such that tip/tilt will not result in decenter.

- **Cost**: Manufacturing the focusing mirror will be more expensive, as the mirror needs to be an off-axis parabolic mirror to focus the spot without aberrations.

- **Availablity**: Concept A and B are made from available or easily manufacturable components. Concept C, however, needs to have a newly designed FSM, to achieve the same optical performance as the other concepts.

5.2.1. Incoming angle

The incoming angle of the beam on the FSM is a design parameter. Theoretically, this angle can be chosen anywhere between 0 and 90 degrees. However, the physics of the design limit it from being too small. If the angle is 0, you cannot focus the beam into the fiber, as the incoming light is blocked. On the other hand, a too large of an angle will also not work. The incoming beam is projected as an oval on the FSM dependent on the incoming angle. If the beam diameter is 10 mm (and the FSM diameter is 18 mm), an angle of 60 ° will result in an oval that is larger than the FSM, which is not desirable. Other than that, smaller angles result in a more compact system. Choosing the incoming angle between approximately 30° and 50° will yield different designs that are all feasible. However, as the more compact design is preferred, the design is chosen to be 30°.

Conclusion

Optically, lenses and mirrors have roughly the same performance. It turns out that mirrors are more likely to meet the space requirements, as a more compact design can be chosen that will survive the launch and space environments more easily. Achieving proper surface roughness is possible for both elements, although it will be more expensive for the mirror. However, cost does not outweight the advantages that mirrors have. It is concluded mirrors outperform lenses, so a mirror is chosen as converging element. Concept C is a promising concept, but a new FSM needs to be designed and tested. Therefore, Concept B will be chosen. The focal length of the mirror is 46.7 mm to guarantee the proper spot size. The incoming angle will be 30°. The orientation of optical components is shown in Figure 5.3.

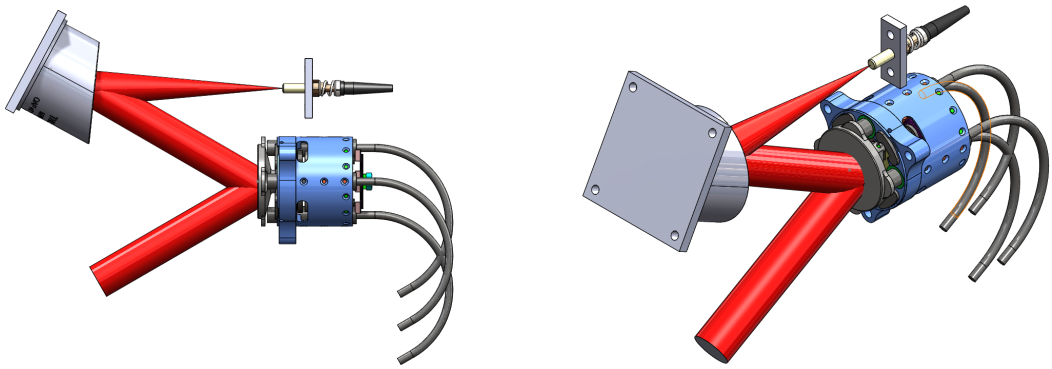

(a) Side view

(b) Isometric view

Figure 5.3: Orientation of optical elements

5.3. Optomechatronic requirements

Here, the effect of misalignment of the chosen components will be discussed. A tolerance analysis will be done for the spot position, and then for all components. This will show if the components can be mounted on manufacturing tolerances, or if an alignment plan will be needed.

5.3.1. Sensitivities of spot position

Here, the sensitivities for the spot position will be determined. Any translation or rotation of the spot will result in a loss of performance, and this needs to be quantified. Tolerances are characterized as decenter (δx,δy), defocus (δz), tip/tilt (δrx, δry) and rotation (δrz). As the spot is rotationally symmetric, (δrz) will not influence performance in any way. Figure 5.4a to Figure 5.4c show the performance drop due to decenter, defocus and tip/tilt .

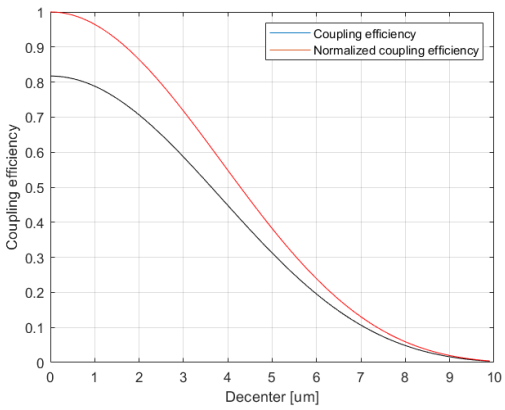

(a) Loss of performance over decenter

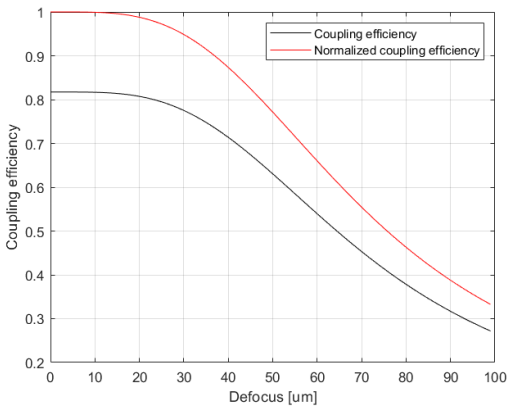

(b) Loss of performance over defocus

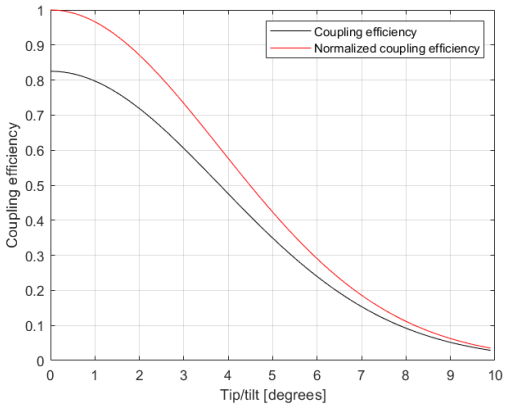

(c) Loss of performance over tip/tilt

Figure 5.4: Performance drop over spot deviations

As can be seen, decenter is the most critical sensitivity. However, the Extremum Seeking Control algorithm will correct for decenter. This means that, as long as the spot is within range of the FSM, decenter will not have effect on performance. The range of the FSM is ±1.5°, the focal length 46.7 mm, so a decenter of 1.3 mm can be accounted for. As it is not desirable for the FSM to operate in its outer range, we will tighten this tolerance to 1 mm. Table 5.2 shows the maximum allowable deviation in all degrees of freedom.

Degree of freedom	**Name**	**Tolerance**
Rx	X-tilt	1°
Ry	Y-tilt	1°
Rz	Rotation	-
Tx	X-decenter	1 mm
Ty	Y-decenter	1 mm
Tz	Defocus	20 µm

Table 5.2: Tolerances on spot position

If movement in multiple degrees of freedom are simultaneously imposed on the system, this might result in crosstalk. The effects of tilt on decenter and defocus are shown in Figure 5.5.

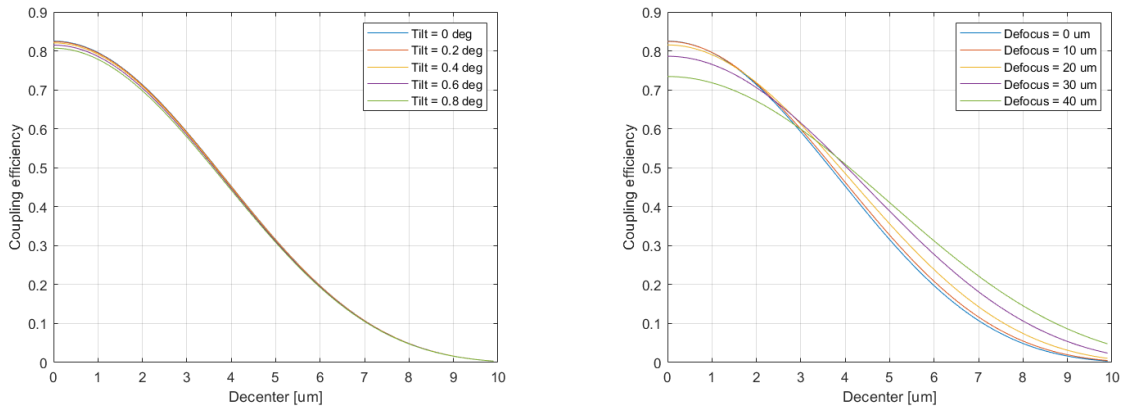

(a) Loss of performance over decenter for various tilts

(b) Loss of performance over defocus for various tilts

Figure 5.5: Performance drop over spot deviations

Figure 5.5a shows that tilt and decenter combined deteriorate performance. However, the effects do not seem to be correlated. That is, a tilt in the system does not make the decenter more sensitive. In Figure 5.5b it can in fact be seen that a defocus actually makes the decenter less sensitive. This is because the spot will become larger due to the defocus, which means larger deviations result in the same performance loss due to decenter. Tip/tilt and defocus show the same uncorrelated behaviour as Figure 5.5a. As long as the deviations due to manufacturing and alignment stay below the tolerances, the positioning requirements will be met.

5.3.2. Sensitivity for individual components

Here, the degrees of freedom of all components will be analyzed, and effect on spot tolerances will be calculated. For the fiber it is simple, as its reference frame corresponds 1 to 1 with the spot position. Manufacturing tolerances of 50 μm will be assumed, to see if the design falls within specifications. If not, the manufacturing tolerances need to be tightened, or an alignment plan will be needed. For angular tolerances, the geometry of each component is taken into consideration. For example, if an object has a manufacturing tolerance of 50 μm and is 25mm long, the maximum tilt angle will be:

$$tilt = \sin^{-1}\left(\frac{0.1}{25}\right) \approx 0.23°$$

The effect of translation and rotation of the parabolic mirror on the spot position is shown in Table 5.3.

-	**Rx** [°]	**Ry** [°]	**Rz** [°]	**X [mm]**	**Y [mm]**	**Z [mm]**
FM rx	2rx	0	0	0	f·sin(2rx)	f·(cos(2rx)-1)
FM ry	0	2ry	0	f·sin(2ry)	0	f·(cos(2ry)-1)
FM rz	0	0	0	f·tan(rz)	0	0
FM x	0	-sin(x/f)	0	x	0	0
FM y	(f·sin(α)+y)/(f·cos(α))-α	0	0	0	y · cos(α)	y · sin(α)
FM z	(f · sin(α) + z · tan(α))/f · cos(α) − α	0	0	0	z · sin(α)	z · cos(α)

Table 5.3: Spot sensitivities due to focusing mirror

Here lowercase rx, ry, rz, x, y, z are rotations and translations of the focusing mirror. Uppercase Rx, Ry, Rz, X, Y, Z are rotations and translations of the spot. α is the incoming angle of the beam, 30° in our case. All rotations are in degrees, all translations in mm. For manufacturing tolerances, this will result in the following:

-	**Tolerance**	**Rx** [°]	**Ry** [°]	**Rz** [°]	**X [mm]**	**Y [mm]**	**Z [mm]**
FM rx	0.23	0.46	0	0	0	0.4	0
FM ry	0.23	0	0.46	0	0.4	0	0
FM rz	0.16	0	0	0	0.13	0	0
FM x	0.05	0	0.05	0	0.05	0	0
FM y	0.05	0.05	0	0	0	0.04	0.02
FM z	0.05	0.02	0	0	0	0.02	0.04
RSS	-	0.46	0.46	0	0.42	0.40	0.05

Table 5.4: Spot sensitivities due to the focusing mirror

The same can be done for the FSM, giving Table 5.5 and Table 5.6.

-	**Rx** [°]	**Ry** [°]	**Rz** [°]	**X [mm]**	**Y [mm]**	**Z [mm]**
FSM rx	$\sin^{-1}(\tan(rx))$-rx	0	0	0	-f·sin(2rx)	f·(cos(2rx)-1)
FSM ry	0	$\sin^{-1}(\tan(ry))$-ry	0	f·sin(2ry)	0	f·(cos(2ry)-1)
FSM rz	0	0	0	0	0	0
FSM x	0	0	0	0	0	0
FSM y	0	0	0	0	0	0
FSM z	$\sin^{-1}(z \cdot \tan(\alpha)/f)$	0	0	0	0	0

Table 5.5: Spot sensitivities due to the FSM

-	**Tolerance**	**Rx** [°]	**Ry** [°]	**Rz** [°]	**X [mm]**	**Y [mm]**	**Z [mm]**
FSM rx	0.22	0.05	0	0	0	0.4	0
FSM ry	0.22	0	0.05	0	0.4	0	0
FSM rz	0	0	0	0	0	0	0
FSM x	0.05	0	0	0	0	0	0
FSM y	0.05	0	0	0	0	0	0
FSM z	0.05	0.02	0	0	0	0	0
RSS	-	0.07	0.05	0	0.56	0.56	0

Table 5.6: Spot sensitivities due to the FSM

Without an alignment plan, the RSS of these components is given below:

-	**Rx** [°]	**Ry** [°]	**Rz** [°]	**X [mm]**	**Y [mm]**	**Z [mm]**
Fiber	0.57	0.57	-	0.05	0.05	0.05
Focusing Mirror	0.47	0.47	-	0.41	0.41	0.1
FSM	0.07	0.05	-	0.56	0.56	0
Total	0.74	0.74	-	0.7	0.7	0.14
Reference	1	1	-	1	1	$20{\cdot}10^{-3}$

Table 5.7: Total component sensitivities

The component sensitivities for each degree of freedom are added quadratically. Note that the decenter (X, Y tolerance) are within the range of the FSM and can be corrected for due to the algorithm. The tip/tilt fall in range and can be expected to account for a loss of efficiency of approximately 3% in total. As only the z-axis does not fall within specification, it makes most sense to devise an alignment plan for this axis, rather than tightening all manufacturing tolerances. Note that with a bit of effort, it is also possible to decrease the manufacturing tolerance, for example by using fitting rings. The reason it was not chosen to do this is twofold. First, it is more expensive and cumbersome to manufacture a system on tighter tolerances. Secondly, the focal length of the converging optic can also deviate, still resulting in a defocus of the spot. In this case, an alignment plan for the z-axis remains necessary. The only efficiency this enhanced system might win is

the tip/tilt, which currently amounts to a loss of approximately 3%. It is decided this would not benefit the coupling loss budget much, so the manufacturing tolerances of 50 μm are kept.

5.4. Final design

As was shown with the tolerance analysis, an alignment plan for the z-axis of the spot is necessary. The manufacturing of the system will be discussed here as well.

5.4.1. alignment of z-axis

The easiest way to align the z-axis is by using shims. Normally, the beam is coupled into the fiber and efficiency can be measured. However, in alignment, it is more advisory to send a beam from the fiber towards the parabolic mirror. If it is perfectly aligned, collimated light comes out. If it is not, the outgoing beam will be either converging or diverging. The rate of this convergence or divergence directly relates to the amount of defocus. Measuring the convergence gives the amount of defocus. Then, shims with this thickness are places between the fiber and housing, such that there is no more defocus. Of course, this can be checked again to see if the outgoing light is collimated. The z-axis can be aligned below 5 μm accuracy with shimming, which results in a remaining coupling efficiency of .99%.

5.4.2. Material choice

Both the housing and the off-axis parabolic mirror will be made from aluminium. This is suitable for space as it is low-weight, and is easily machinable. Its high thermal conductivity will also result in low thermal gradients. In particular, the aluminium 7000 series has proven to be suitable for space applications due to its high yield strength. Aluminium 7075T6 will be chosen as an initial material choice. As both housing and focusing mirror expand homogeneously, there will be no internal stresses in this part, and no change of focus. The FSM is made of 301-steel, so between FSM and housing thermal loads might induce stress. The relevant parameters for said materials are shown in Table 5.8.

Table 5.8: Material properties of components

Material	Thermal expansion coefficient	Yield strength
Aluminium 7075T6	21.6 μm /m°C	503 MPa
Steel 301	16.6 μm /m°C	205 MPa

5.4.3. Manufacturing

Figure 5.6 shows the optical design, where the housing is kept solid (left) and transparent (right). In Appendix A, more figures of the optical design are shown, to see more detail.

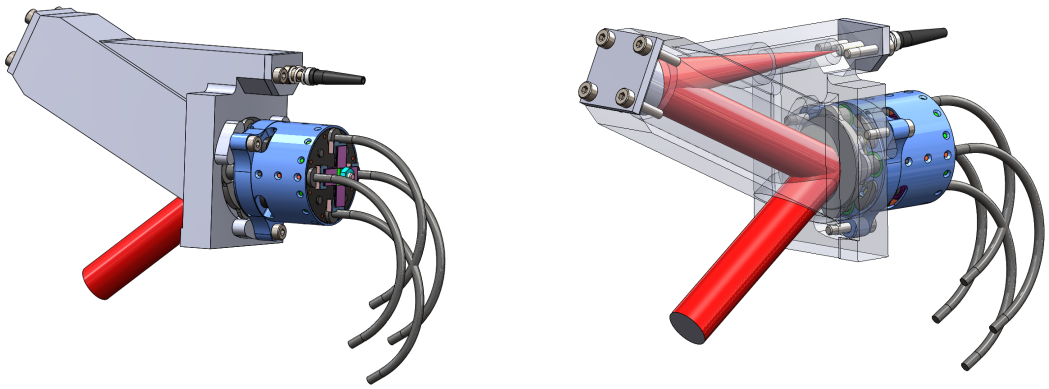

(a) Isometric view of design

(b) Design with transparent housing

Figure 5.6: Orientation of optical elements with housing

The red cylinder represents the laser with a diameter of 10 mm. The laser first hits the FSM, then the off-axis parabolic mirror and finally the fiber. The housing is made by milling the outer structure. After this,

cylindrical holes are drilled such that the beam can pass through it. As the beam converges towards the fiber, the holes will become smaller in a stepwise manner. It is assumed the manufacturing tolerances are 50 µm. All components will be bolted down with M2-12.9 bolts. The angle between FSM and focusing mirror is 30 °. The connection between housing and fiber is shown below.

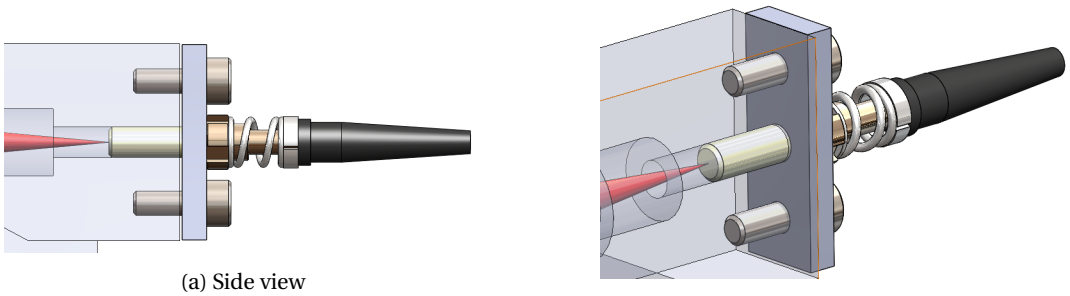

(a) Side view

(b) Isometric view

Figure 5.7: Orientation of optical elements with housing

The fiber will be glued to a small aluminium slab. This slab is then bolted to the entire structure, with shims in between. While outgassing of adhesives is an issue in space, there are various adhesives suitable for this application. The design of the fiber connector is based on the design of the current system in TNO, which also makes use of an adhesive between fiber and housing.
The housing is designed to be as light-weight as possible, while still being manufacturable with milling and drilling. It is assumed the same mirror, FSM and fiber are used. However, in the original design one beam-splitter and the position sensor are necessary as well, resulting in more weight.
This design meets all optical requirements. Whether the system will meet the thermal and vibrational requirements will be shown in Chapter 6 and Section 6.2, respectively.

5.5. Conclusion

A design was made that meets all optical requirements. A tolerance analysis was done that shows alignment plan is needed for the z-axis of the spot. Even with a wide margin, all other components can be mounted on manufacturing tolerances. The alignment will be done with shimming. A coupling loss of 6% can be expected due to tip/tilt. Other degrees of freedom will not result in loss of efficiency.

6

Thermal and vibrational stability

This chapter discusses if the thermal requirements imposed on the design can be met. The satellite is subject to two thermal load cases. As the FSM and housing are made from a different material, internal stresses might occur due to these load cases. While these stresses do not influence spot performance, they might result in material fatigue or thermal snapping. Furthermore, internal satellite vibrations might also deteriorate performance. Section 6.1 analyses the thermal stability of the design, Section 6.2 the vibrational stability. Section 6.3 concludes this chapter.

6.1. Thermal stability

6.1.1. Thermal load cases

There are two main load cases considered for functioning of the fiber coupler. The first is a singular homogeneous temperature drop of 70 °C, which occurs when the satellite is sent into orbit and before it is operational. TNO standards indicate machinery should be able to survive minimum temperatures down to -50 °C, and it is assumed mounting and alignment is done at 20 °C. Secondly, during operation, the satellite will circle around the Earth. It will reach its highest temperatures when it is subjected to solar radiation and lowest temperatures when it is in the shadow of the earth. Due to thermal control of the satellite, this thermal cycle is estimated to be between -20 °C and 40 °C. The materials must not plastically deform and must not show fatigue due to continuous deformation or thermal snapping. It is assumed a continuous subjection of 20% of the yield strength of the materials will lead to fatigue. The two load cases are summed up in Table 6.1.

Table 6.1: Thermal load cases on the subsystem

Load case	Von Mises stress	Thermal snapping
One-time temperature drop of 70 °C	100% of yield strength	Allowable
-20 °C to 40 °C thermal cycle	20% of yield strength	Not allowable

Note that one-time thermal snapping will not lead to loss of performance, as the spot tolerances are not influenced by the FSM's degrees of freedom. Only continuous thermal snapping will lead to fatigue in the material, which might lead to material failure.

6.1.2. Designing for compliance

This section discusses how the design can account for thermal effects. The design is made compliant between FSM and housing, such that movement between FSM and housing will be allowed in certain directions. This should result in lower stresses in the system, and prevent thermal snapping. The stress between the housing and FSM occurs radially, which is away from the thermal center. Because the connection has lower stiffness than the rest of the housing, movement is allowed up to a certain degree. The desired movement between the housing and FSM on the connection points can be computed by Equation (6.1).

$$d = (CTE_{al} - CTE_{st}) r T \tag{6.1}$$

Here, d is the relative movement away from the thermal center in μm. r is the distance from thermal center to each connection point, which is 14.4 mm. The temperature drop T is 40°, which means the relative movement is 2.88 μm. As long as the housing allows for this movement, thermal snapping will not occur and stresses in the FSM should be low enough. Figure 6.1 shows the connection between FSM and housing more clearly.

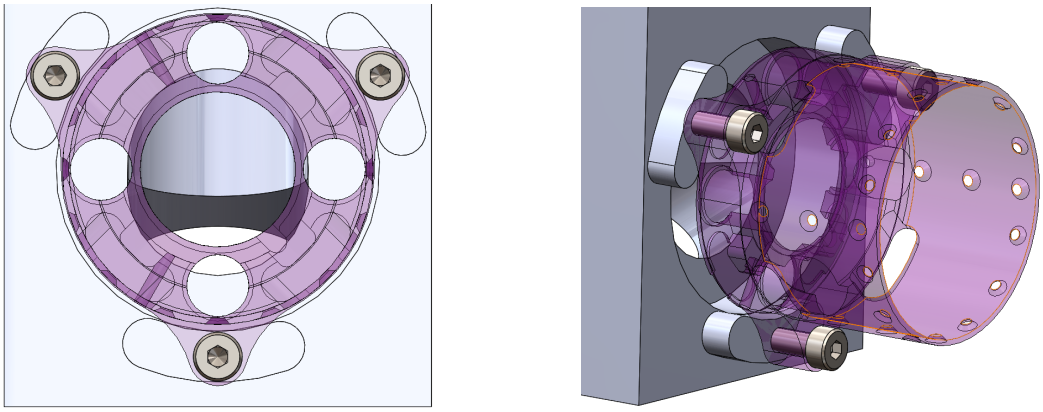

(a) Front view

(b) Isometric view

Figure 6.1: Flexure design of mounting the FSM to the housing

There are three islands that stick out of the housing. As they are relatively thin, they allow for the flexibility needed by the expansion. Note that the compliant connections are at angles 0°, 60° and 120° with respect to the vertical axis. This way, if the FSM expands relative to the housing, all movement away from the center is tolerated.

Thermal snapping

Thermal snapping occurs when two different materials are mounted together. Due to a temperature change, the two materials expand at a different rate, resulting in a shear force, F_s, along the surfaces. A static friction force, governed by Equation (6.2), holds the two materials in place as long as it is higher than F_s.

$$F_\mu = \mu F_N \tag{6.2}$$

Here F_μ is the friction force, μ the friction coefficient between the two materials and F_N the normal force imposed by the bolts. When the shear force exceeds this friction force, it will start to move. As static friction is higher than dynamic friction, the materials will keep moving until the stresses are reduced to the dynamic friction value. Continuous snapping will cause the materials to wear, which is not desirable.

The amount of normal force is dependent on the bolt type and size. The FSM supports M2 bolt holes. The highest proof load is achieved with M2-12.9 and is 2130N. As this system works in a dry environment, the friction coefficient between aluminium and steel can be expected to be 0.61. This means a clamp load of around 800N can be expected. This puts the maximum static friction force that can be achieved at 488 N. The shear force must not exceed 488 N. This force must result in at least 2.88 μm deformation. Thus, the maximum stiffness in the connection can be calculated with Equation (6.3).

$$k < F/u = 1.7e8N/m \tag{6.3}$$

Where F is the force applied and u is the deviation. If the (local) stiffness is higher, the material deformation of 2.88 μm will result in a force that exceeds 488N, meaning thermal snapping will occur.

By iterating between design and measurement of connection point stiffness, the design is given its proper compliance. This is shown in Figure 6.2.

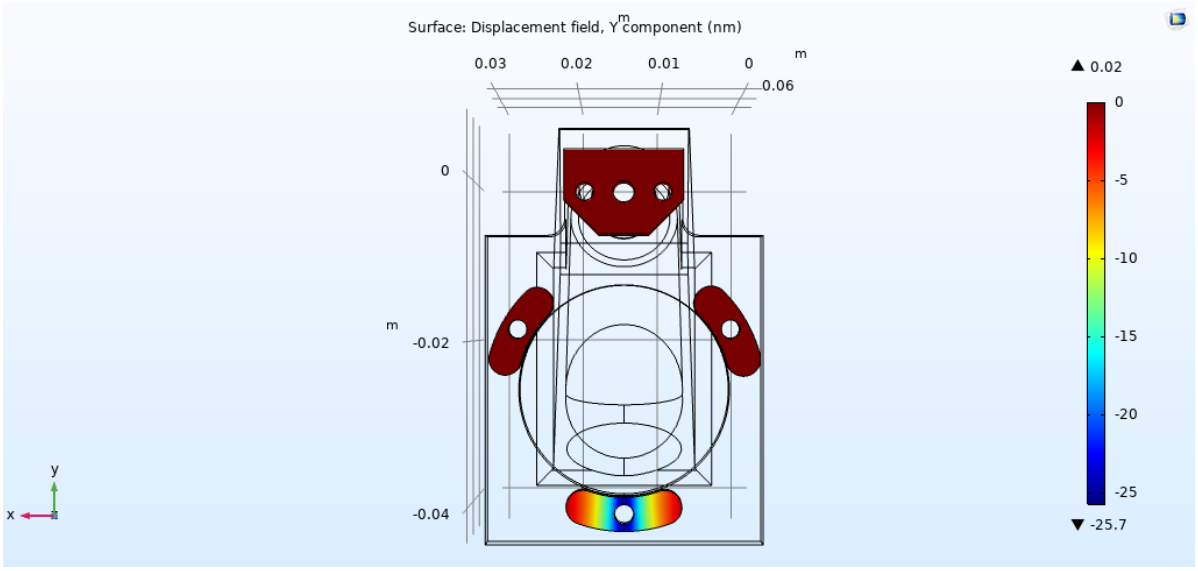

Figure 6.2: Deflection of structure in nm due to 1 N load.

Here, a load of 1 N is applied at the bottom connection. The maximum vertical deflection due to this load is 25.7 nm. This would mean the connection points have a stiffness of roughly 3.8 e7 N/m. This is a factor 5 lower. It is expected thermal snapping will not occur. Section 6.1.4 analyses the second thermal load case, to verify this.

6.1.3. Load case one

When the system cools down, the aluminium housing will shrink at a faster rate than the steel. As they are bolted together, internal stresses will occur. If the maximum Von Mises stress exceeds the yield strength at any place in the material, plastic deformation will occur. As the highest stresses occur near the boundary between the FSM and aluminium housing, it is advisory to zoom in on that area. The surfaces of both FSM and housing will be subjected to the same analysis, and are shown in Figure 6.3 and Figure 6.4. Note that only the housing of the FSM will be taken into this simulation. It is assumed that if the housing does not succumb to material fatigue, the entire FSM will not.

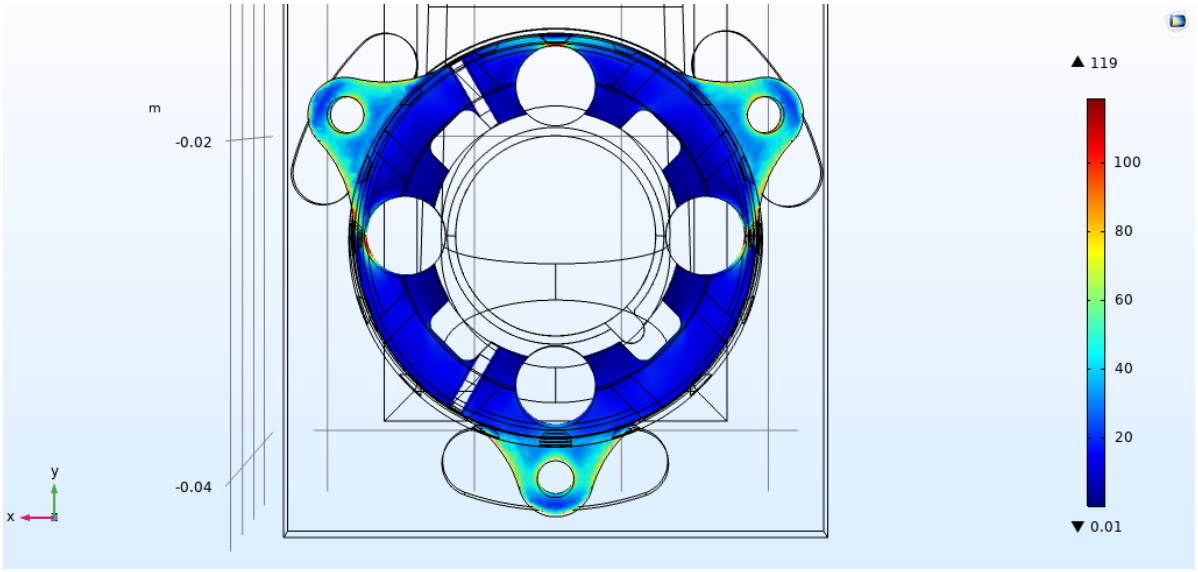

Figure 6.3: Von Mises stress in FSM

The maximum von Mises stress is 119 MPa, occuring at the thin left and right boundaries of the housing. As the yield strength of steel is 205 MPa, there will be no plastic deformation. Other than the small edges in the

FSM housing, the highest stresses occur near the bolt holes. The stress profile in the edge of the aluminium housing is shown in Figure 6.4.

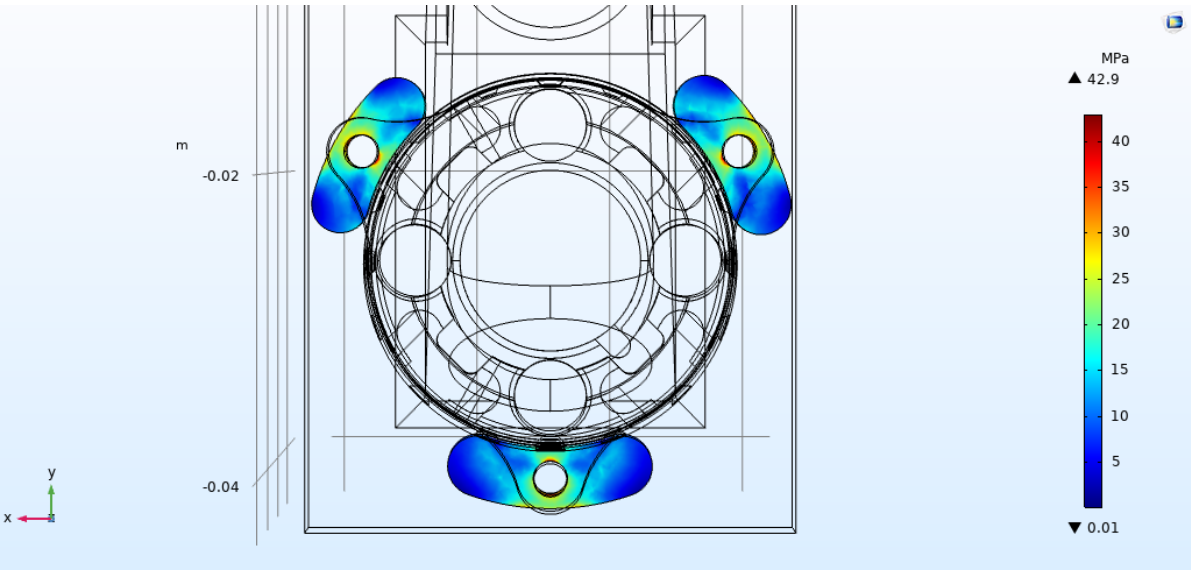

Figure 6.4: Von Mises stress in aluminium housing

As the housing is thicker, its stresses are more evenly distributed and find a maximum around the edges of 42.9 MPa. Again, this does not reach the regions of plastic deformation. The first load case imposes no problem on the design, which means before operation the system will remain intact.

6.1.4. Load case 2: Thermal cycling

It is assumed the mounting will be done in room temperature conditions, e.g. 20 °C. This means that the satellite will be subject to a temperature drop of 40 °C, and a temperature increase of 20 °C. Both are not allowed to result in thermal snapping. Furthermore, the Von Mises stress should not exceed 20% of the yield strength of the materials. Figure 6.5 and Figure 6.6 show the von Mises stresses due to a temperature drop of 40 °C for the FSM and housing, respectively. The same is done for an increase of 20°.

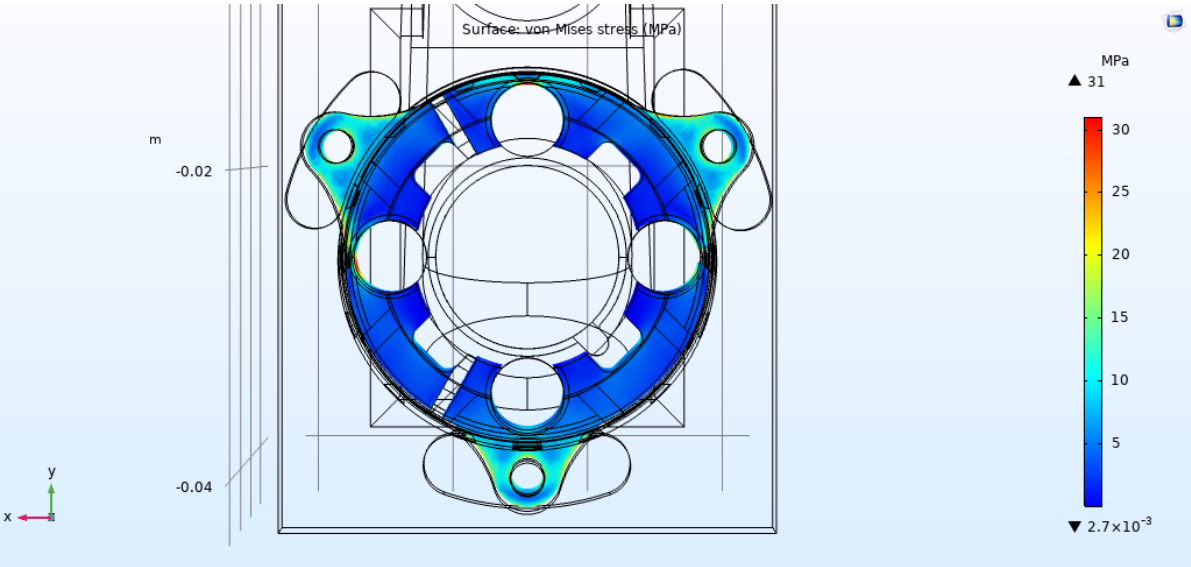

Figure 6.5: Von Mises stress in FSM, due to 40 °C temperature drop

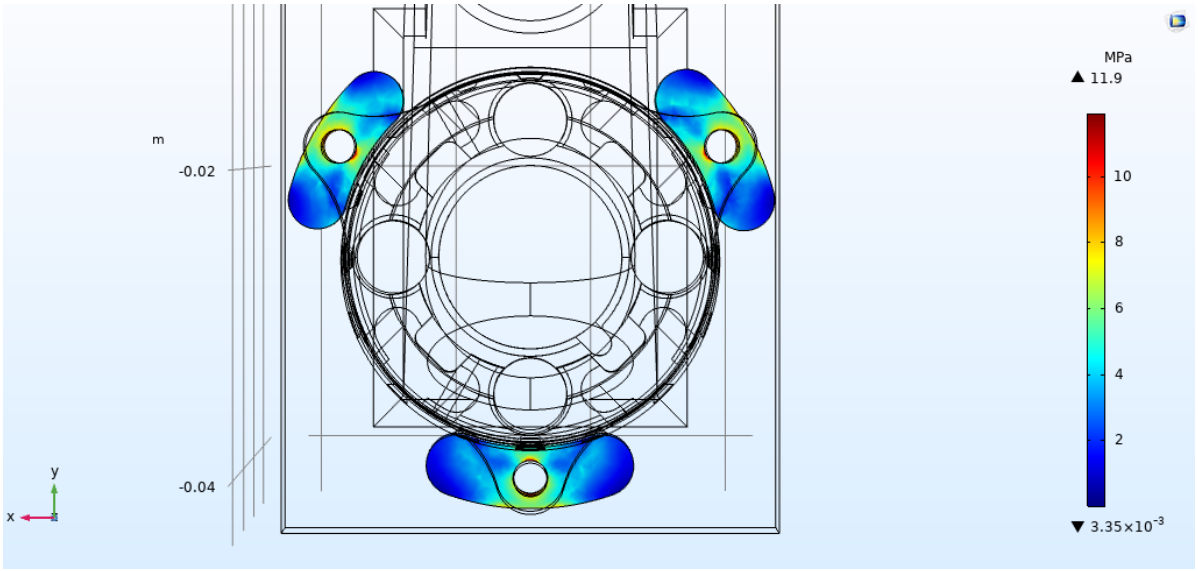

Figure 6.6: Von Mises stress in aluminium housing, due to 40 °C temperature drop

For the FSM, the maximum measured stress is 31 MPa, which is 15% of the yield strength. For the aluminium, 11.5 MPa equals approximately 3% of the yield strength. For the studies of a temperature increase of 20 °C, the these values are 8% and 2% for the FSM and housing respectively. The simulation was done with various mesh sizes, of which all yielded approximately the same results. Both values stay below 20% of the yield strength, meaning no material fatigue will occur in the long run.

It is difficult to find the amount of shear stress along the surfaces to see whether thermal snapping will occur. An estimation is done by assuming all the von Mises stress is in the shear direction. The average von Mises stress in a connection point is approximately 10 N/mm^2, which is already a worst case scenario. As the surface between FSM and housing is around 14 mm^2 for each connection, the total shear force will be approximately 140 N. This is below the 488 N, so it is expected that thermal snapping will not occur. The reason this value is so much lower that the maximum allowable shear force, is that the three island provide a lot of compliance. As was mentioned above, the stiffness of the connection was a factor X lower than was necessary.

6.1.5. Findings

Due to the compliance between housing and FSM, thermal snapping will not occur and the von Mises stresses will not result in plastic deformation or material fatigue. This means the optomechanical design meets the thermal requirements.

6.2. Vibrational analysis

This section discusses the if the design can meet the vibrational requirements. The goal is to determine if the vibrations imposed on the system will lead to loss of optical performance. To determine this, an eigenmode analysis of the design will be done. When the eigenfrequencies are known, the vibrations at those frequencies are analysed to see if the system is subject to component deviations. These deviations can then translated to coupling loss by consulting Figure 5.4.

The subsystem is connected to the rest of the telescope. Any vibrations will be transferred to this system through the connection. The blue part shown in Figure 6.7 is chosen as the connection and modeled as a fixed constraint. Note that as this project only focuses on the fiber coupling subsystem, the rest of the satellite is not modeled around it. How the systems will be connected will vastly differ per satellite, so this is merely an indication.

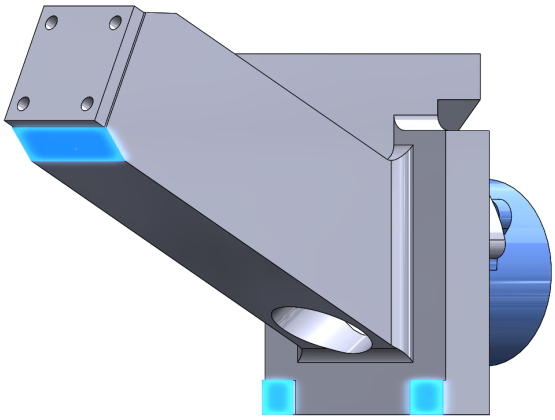

Figure 6.7: Connection between satellite and housing (blue)

The mass and center of mass of the FSM are known. For simplification, the FSM is modeled as a block with these parameters. The first two eigenmodes are shown in Figure 6.8.

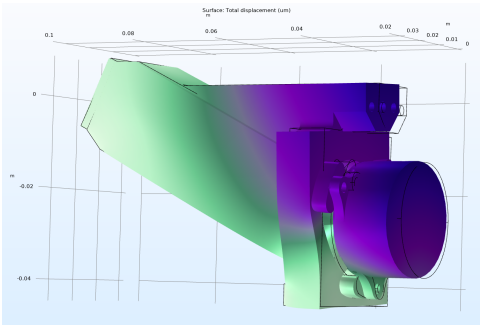

(a) First eigenmode at 4194.4 Hz

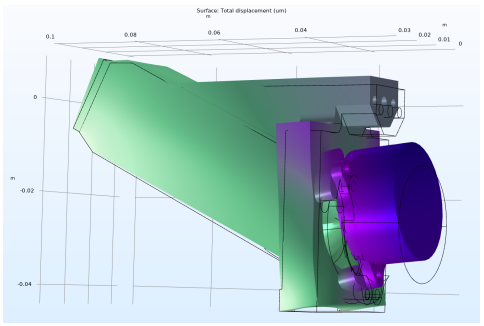

(b) Second eigenmode at 6200.6 Hz

Figure 6.8: Eigenmodes of the housing

The first eigenmodes are at 4194.4 Hz and 6200.6 Hz. Note that the extremum seeking control does not work at these frequencies, so it must be determined what coupling loss is expected here. To determine the amplitude of vibrations at these frequencies, Figure 4.3a is consulted. The vibrations according to the ESA-spec will be chosen, as it is used within TNO. This can be modeled as a low pass filter with a corner frequency of 10 Hz. The first eigenmodes are so high that they do not show up on the chart, but with the low pass filter they can be estimated. The square root of the surface of this value determines the root mean square amplitude of vibrations.
The amplitude of vibrations at 4194.4.6 Hz and 6200.6 Hz are approximately 0.04 μm and 0.03 μm. Figure 6.8a show that the main direction of movement is a decenter of the fiber. However, 0.04 μ decenter result in virtually no coupling loss, as can be checked in Figure 5.4b. Figure 6.8b shows that the second eigenmode results mainly in a rotation of the FSM. Eventually, this will result in a spot decenter. Again, the amplitude of this decenter is so loss that no loss of performance is expected.

All higher order eigenmodes have even lower amplitudes, so it is assumed that vibrations in orbit will not result in loss of performance due to eigenmodes. However, the entire satellite will vibrate with characteristics described in Figure 4.3a. This will result in a tip/tilt at the entrance aperture. The influence of satellite vibrations on control performance will be discussed in Chapter 9.

Findings

Optical performance due to microvibrations in orbit is investigated by looking at eigenfrequencies of the coupling subsystem. It is concluded that the characteristics and frequency of eigenmodes is dependent on the point of contact of the satellite. The eigenfrequencies are desired to be as large as possible, such that

vibrations diminish. The chosen system connection leads to a first eigenfrequency at 4194.4 Hz, which leads to virtually no loss of performance due to eigenmodes.

6.3. Conclusion

The optical design was subjected to two thermal load cases. Under these conditions, the design must not succumb to material fatigue and thermal snapping. As the FSM and housing are from different materials, a temperature deviation will result in internal stresses. By making the housing compliant, the stresses in the FSM and housing do not exceed the values imposed by the load cases. This means the thermal requirements are met.

An eigenmode analysis was done to see if any eigenfrequencies lead to loss of optical performance. The eigenfrequencies where so high, that the amplitude of these vibrations were considered to have no effect on optical performance.

7

Extremum Seeking Control: algorithm description and stability

7.1. Introduction

Here, Extremum Seeking control is explained, as well as how extremum Seeking Control works in fiber coupling. After this, a stability analysis is done for a general Extremum Seeking Control scheme with a Gaussian objective function.

Principles of ESC

Extremum Seeking Control is a control law that is able to find an extremum in a slowly changing system, without modelling or measuring them.

The power of Extremum Seeking lies in that a model of the system is not necessary. It only needs an objective function that can be maximized or minimized. In the case of fiber coupling, it is not required to know the position of the spot and fiber. As long as intensity measurements are available, the system can find a maximum. Furthermore, it can adapt to slowly changing parameters, without losing its efficiency. As was discussed earlier, the fiber can slowly drift due to thermal effects, but the control algorithm can keep up with these changes as long as they are relatively slow.

In fiber coupling, there is one maximum coupling efficiency, when the center of the spot and the fiber coincide perfectly. All deviations from this point will result in a lower efficiency. ESC is able to find the maximum efficiency by moving around its current position and measuring the corresponding intensity. If the intensity increases, the direction of movement is correct and a positive feedback will be given. How the feedback system works is explained below. Figure 7.1 shows an initial, suboptimal position $\hat{u}$ of the algorithm.

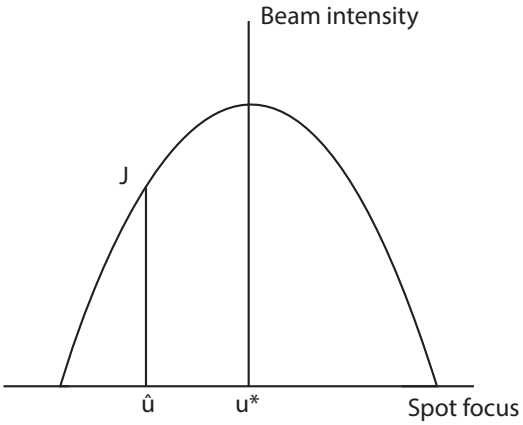

Figure 7.1: Starting point of ESC algorithm

To find the optimal position u^* and thereby the maximum intensity, the control law is going to add a sinusoidal perturbation. The input is hereby shifted to the left and right. In doing so, the intensity is going to fluctuate as well. This is illustrated in Figure 7.2.

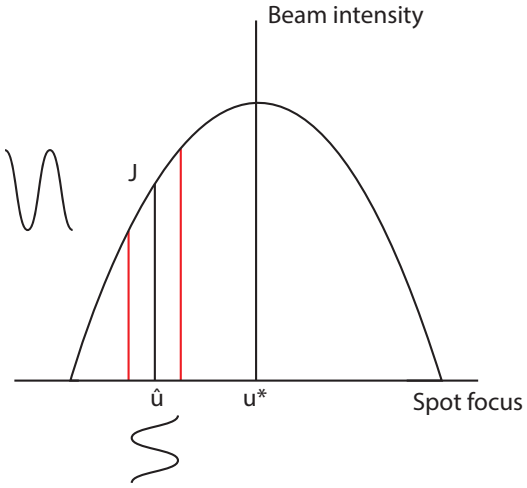

Figure 7.2: Observed output with perturbed input

Note that the sine waves of input and output have the same frequency by default, and must have either equal phase (when the input is to the left of the optimum), or opposite phase (when the input is to the right of the optimum). After all, if you increase the input position if the initial position is to the left of the optimum (e.g. a negative position), the intensity also increases. If you increase the input position if you're to the right of the optimum, the intensity decreases. This observed output might have some phase delay, ϕ, but for now this is not taken into consideration. The two possible situations are shown in Figure 7.3 and Figure 7.4:

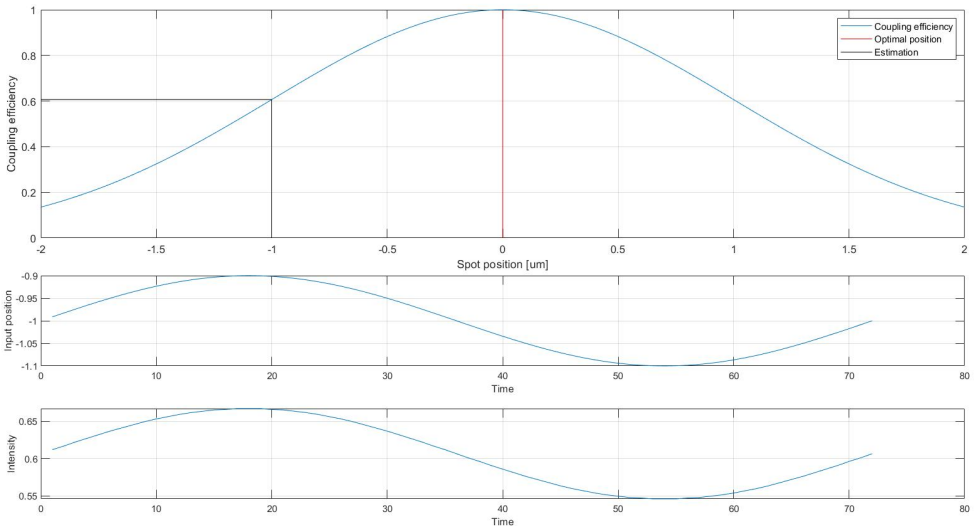

Figure 7.3: Negative initial position

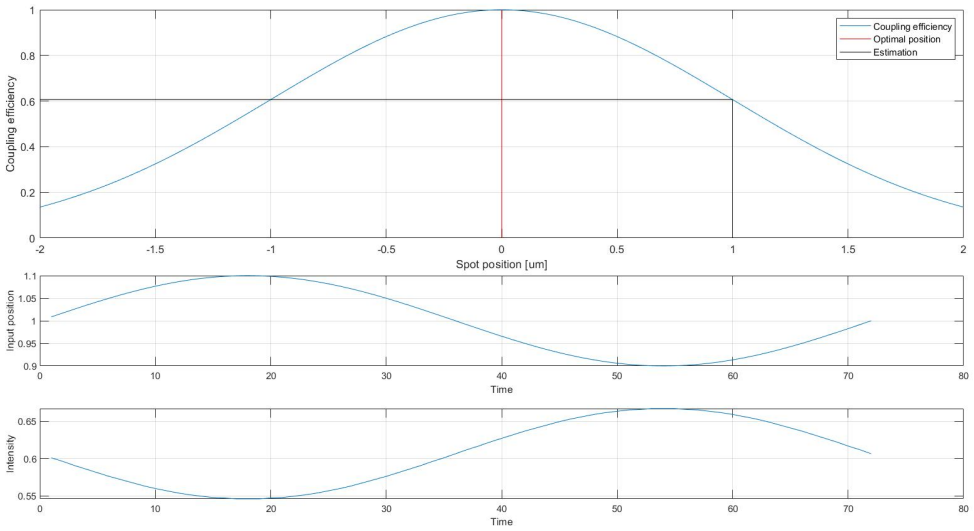

Figure 7.4: Positive initial position

In both figures, the top subfigure again shows the intensity over position. The middle figure shows that the position is moving sinusoidally around its starting position (-1 µm and 1 µm, respectively). For these positions, the corresponding intensity is shown in the bottom subfigure, and fluctuates between 0.55 and 0.65.

In case 1, the input is to the left of the optimum, in case 2 is it to the right. If the mean value is subtracted from each signal, such that the oscillations of intensity occur around 0, and the product is taken between the input and output, the result is a purely positive signal (case 1) or a purely negative signal (case 2). See Figure 7.5:

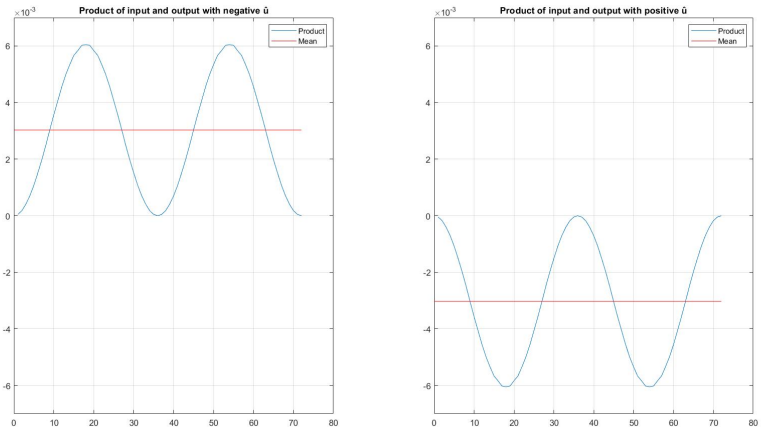

Figure 7.5: Product of input and output in two cases

This resulting signal is to be averaged (such that it does not oscillate as much) and fed back to the system. A positive feedback will drive the input to the right, a negative feedback will drive it to the left. Either way, it is converging to an optimum. In the case the optimum has been found, the resulting feedback will look like this.

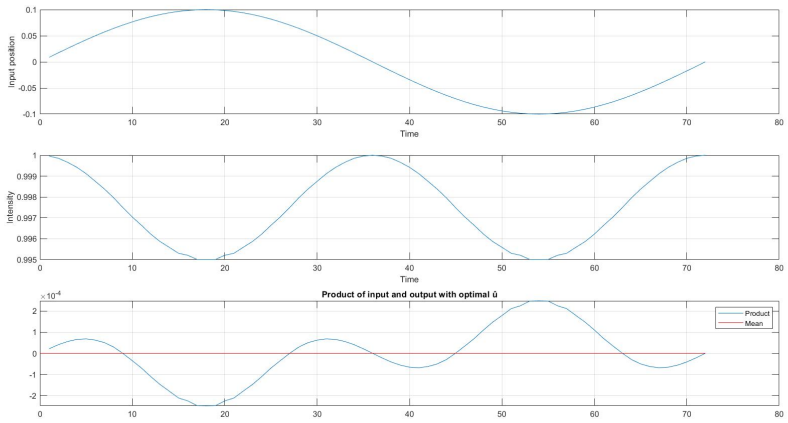

Figure 7.6: Feedback signal

This shows the resulting signal will be partly positive and partly negative, which would average out to 0. Furthermore, it can be seen that the slope at the initial position will influence the magnitude of the outgoing signal. In case of a high slope, the feedback signal will be higher and the algorithm will converge faster to an optimum. When the signal is closer to the optimum, the feedback will also decrease in magnitude. Around the optimum the feedback is lowest (which can be seen by comparing Figure 7.5 and Figure 7.6).
In the above explanation it was assumed the mean of the intensity can be removed, and signals can be smoothed out. This is done by filtering. Figure 7.7 shows the entire control scheme, and it will be explained where each filter will be applied.

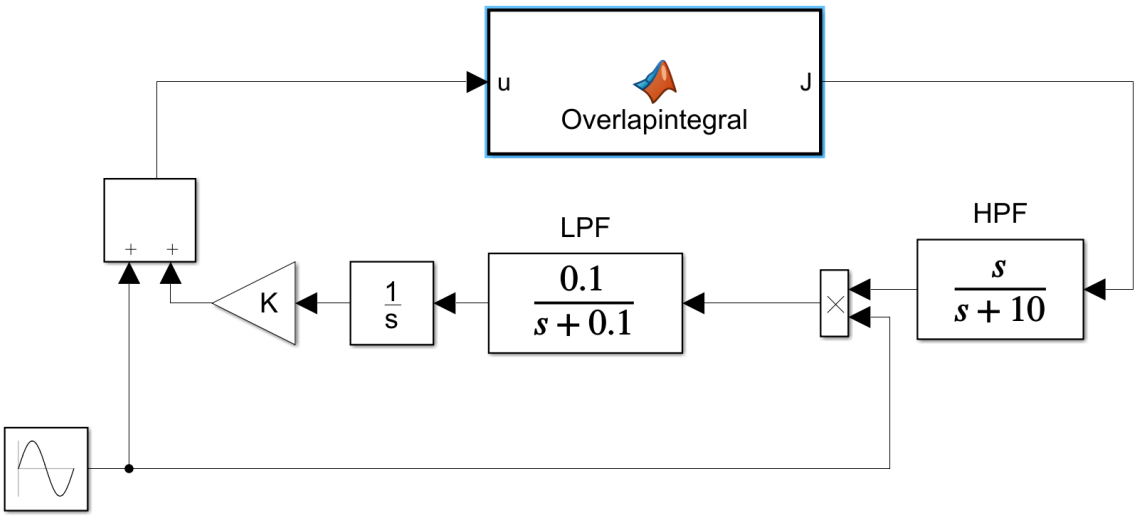

Figure 7.7: Extremum Seeking control scheme

The current spot position is translated to a certain intensity by calculating the amount of overlap between spot and fiber. The overlap is the intensity in the fiber, which is high-pass filtered to remove the mean. After this filter, the product is taken between this intensity and the sinusoidal input. This signal passes a low-pass filter to remove the high-frequency components. This signal is integrated and multiplied with a feedback gain K, which determines the aggressiveness of the algorithm.

7.2. Stability analysis

Below is the proof of stability of the ESC algorithm, when it is applied to a fiber coupling system. This proof of stability holds for any system with a Gaussian objective function. The stability of a quadratic input output

mapping has been proven **??**, but in the case of fiber coupling the mapping is closer to a Gaussian beam, as can be seen in Figure 7.8.

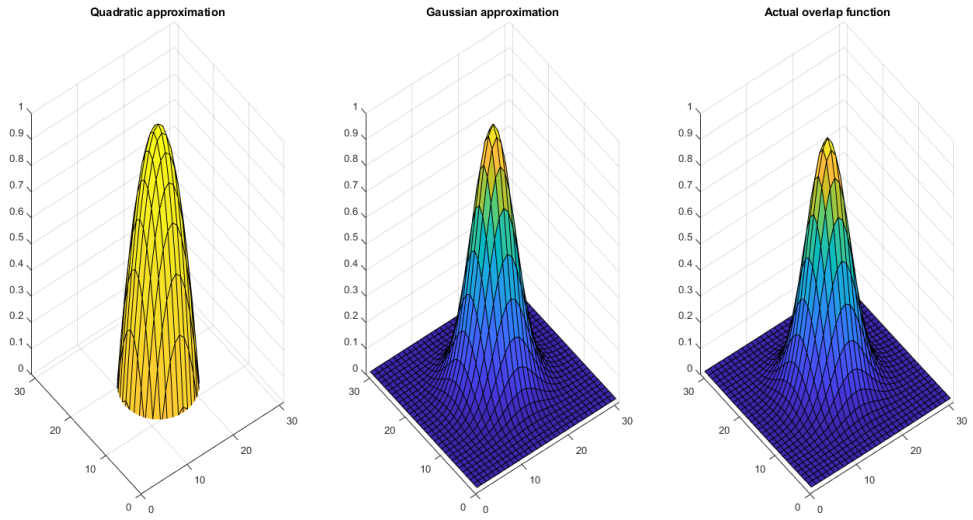

Figure 7.8: Quadratic mapping (left), Gaussian mapping (middle) and actual fiber coupling mapping (right)

Proof of stability for a Gaussian objective function is left below. At first, we still assume the optimal position θ^* to be constant (no fiber movement). The goal is to prove that the estimation error is driven to zero, which means the position is driven to the optimal position. The Gaussian shape as a function of position is determined as:

$$I(\theta) = e^{-\frac{(\theta-\theta^*)^2}{w_r^2}} \tag{7.1}$$

Where w_r is the mode field radius, θ the current position and θ^* the optimum. We use:

$$\theta = \hat{\theta} + asin(\omega t) \tag{7.2}$$

Where $\hat{\theta}$ is the estimation of current position. This is the sinusoidal perturbation with amplitude a and frequency ω. Let $\tilde{\theta}$ be the estimation error, such that

$$\tilde{\theta} = \theta^* - \hat{\theta} \tag{7.3}$$

Which is to say, the difference between the optimal position and current position. This means Eq 7.4 can be rewritten as:

$$I(\theta) = e^{-\frac{(\tilde{\theta}-a\sin(\omega t))^2}{w_r^2}} \tag{7.4}$$

This can be rewritten to sine/cosine terms, after which it is easier to determine which terms drop out due to the filters in the system:

$$y = \cos\left(i\frac{\tilde{\theta} - a\sin(\omega t)^2}{w_r^2}\right) + i\sin\left(i\frac{\theta - a\tilde{\sin}(\omega t)^2}{w_r^2}\right) \tag{7.5}$$

Or

$$y = \cos\left(i\frac{\tilde{\theta^2} - 2a\tilde{\theta}\sin(\omega t) + a^2 sin^2(\omega t)}{w_r^2}\right) + i\sin\left(i\frac{\tilde{\theta^2} - 2a\tilde{\theta}\sin(\omega t) + a^2 sin^2(\omega t)}{w_r^2}\right) \tag{7.6}$$

We will assume a, the dithering amplitude, to be small such that higher order a-terms can be neglected.

$$y = \cos\left(i\frac{\tilde{\theta^2} - 2a\tilde{\theta}\sin(\omega t)}{w_r^2}\right) + i\sin\left(i\frac{\tilde{\theta^2} - 2a\tilde{\theta}\sin(\omega t)}{w_r^2}\right) \tag{7.7}$$

Using series expansions, this will be rewritten as:

$$\cos\Big(i\frac{\tilde{\theta^2}-2a\tilde{\theta}\sin(\omega t)}{w_r^2}\Big)=\Big[1-\frac{i^2\tilde{\theta}^4-4ai^2\tilde{\theta}^3\sin(\omega t)}{w_r^2 2!}+\frac{i^4\tilde{\theta}^8-8ai^4\tilde{\theta}^7\sin(\omega t)}{w_r^4 4!}\Big] \tag{7.8}$$

Where higher order terms of a are again neglected.

$$\cos\Big(i\frac{\tilde{\theta^2}-2a\tilde{\theta}\sin(\omega t)}{w_r^2}\Big)=\Big[1-\frac{i^2\tilde{\theta}^4}{w_r^2 2!}+\frac{i^4\tilde{\theta}^8}{w_r^4 4!}+\frac{-4ai^2\tilde{\theta}^3\sin(\omega t)}{w_r^2 2!}+\frac{-8ai^4\tilde{\theta}^7\sin(\omega t)}{w_r^4 4!}\Big] \tag{7.9}$$

$$\cos\Big(i\frac{\tilde{\theta^2}-2a\tilde{\theta}\sin(\omega t)}{w_r^2}\Big)=\cos(\frac{i\tilde{\theta^2}}{w_r^2})+\frac{2ai\tilde{\theta}\sin(\omega t)}{w_r^2}\big[\frac{i\tilde{\theta^2}}{w_r^2}-\frac{i^3\tilde{\theta^6}}{w_r^6 3!}+...\big] \tag{7.10}$$

$$=\cos(\frac{i\tilde{\theta^2}}{w_r^2})+\frac{2ai\tilde{\theta}\sin(\omega t)}{w_r^2}\sin(\frac{i\tilde{\theta^2}}{w_r^2}) \tag{7.11}$$

Similar expansions yield:

$$i\sin\Big(i\frac{\tilde{\theta^2}-2a\tilde{\theta}\sin(\omega t)}{w_r^2}\Big)=i\sin(\frac{i\tilde{\theta^2}}{w_r^2})+\frac{2a\tilde{\theta}\sin(\omega t)}{w_r^2}\cos(\frac{i\tilde{\theta^2}}{w_r^2}) \tag{7.12}$$

This means Eq 7.7 can be rewritten as:

$$y=\cos(\frac{i\tilde{\theta^2}}{w_r^2})+i\sin(\frac{i\tilde{\theta^2}}{w_r^2})+\frac{2ai\tilde{\theta}\sin(\omega t)}{w_r^2}\sin(\frac{i\tilde{\theta^2}}{w_r^2})+\frac{2a\tilde{\theta}\sin(\omega t)}{w_r^2}\cos(\frac{i\tilde{\theta^2}}{w_r^2}) \tag{7.13}$$

$$y=e^{-\frac{\tilde{\theta}^2}{w_r^2}}+\frac{2a\tilde{\theta}e^{-\frac{\tilde{\theta}^2}{w_r^2}}\sin(\omega t)}{w_r^2} \tag{7.14}$$

Now, applying the High-Pass filter removes the DC-gain, such that:

$$\frac{s}{s+h}[y]\approx\frac{2a\tilde{\theta}e^{-\frac{\tilde{\theta}^2}{w_r^2}}\sin(\omega t)}{w_r^2} \tag{7.15}$$

This is multiplied with asin(ωt), which gives:

$$\xi\approx\frac{2a^2\tilde{\theta}e^{-\frac{\tilde{\theta}^2}{w_r^2}}\sin^2(\omega t)}{w_r^2} \tag{7.16}$$

Again applying $2\sin^2(x)=1-cos(2x)$ gives:

$$\xi\approx\frac{2a^2\tilde{\theta}e^{-\frac{\tilde{\theta}^2}{w_r^2}}}{w_r^2}-\frac{2a^2\tilde{\theta}e^{-\frac{\tilde{\theta}^2}{w_r^2}}}{w_r^2}\cos(2\omega t) \tag{7.17}$$

This passes the integrator:

$$\hat{\theta}\approx\frac{k}{s}\big[\frac{2a^2\tilde{\theta}e^{-\frac{\tilde{\theta}^2}{w_r^2}}}{w_r^2}-\frac{2a^2\tilde{\theta}e^{-\frac{\tilde{\theta}^2}{w_r^2}}}{w_r^2}\cos(2\omega t)\big] \tag{7.18}$$

Because the integrator greatly attenuates high frequency signals:

$$\hat{\theta}\approx\frac{k}{s}\frac{2a^2\tilde{\theta}e^{-\frac{\tilde{\theta}^2}{w_r^2}}}{w_r^2} \tag{7.19}$$

Or

$$\dot{\hat{\theta}}\approx\frac{2ka^2\tilde{\theta}e^{-\frac{\tilde{\theta}^2}{w_r^2}}}{w_r^2} \tag{7.20}$$

As seen before, we assume a static map (so constant θ^*), which means:

$$\dot{\tilde{\theta}} = -\dot{\hat{\theta}} \tag{7.21}$$

Thus,

$$\dot{\tilde{\theta}} = \frac{-2ka^2 e^{-\frac{\tilde{\theta}^2}{w_r^2}} \tilde{\theta}}{w_r^2} \tag{7.22}$$

Now, because k, w_r and $e^{-\frac{\tilde{\theta}^2}{w_r^2}}$ are strictly positive, the estimation error $\dot{\tilde{\theta}}$ is driven to 0, which means the position is driven to the optimum θ^*. This proves stability for a Gaussian mapping where the fiber position is kept constant. In a similar fashion, the estimation is derived for the same mapping but with a moving fiber. The fiber is assumed to move in a sinusoid with amplitude b and frequency ω_0.

$$\dot{\tilde{\theta}} = \frac{-2kae^{-\frac{\tilde{\theta}^2}{w_r^2}} \tilde{\theta}}{w_r^2} + b\omega_0 cos(\omega_0 t) \tag{7.23}$$

7.3. Conclusion

Extremum Seeking control is explained, and how it can be implemented in fiber coupling. The stability of this system is proven for a Gaussian objective function. The next chapters will analyse the control parameters of the algorithm, and the performance under the disturbances imposed on the system.

8

Control Parameters analysis

8.1. Introduction

This chapter shows the influence of all control parameters on system performance. Based on this analysis, the optimal parameters are chosen for this experimental setup. For both a simulink model and the experimental setup, the parameters are tested. There are two parameters that will determine the performance of the algorithm. They are the dithering frequency, ω and the dithering amplitude a. Furthermore, there is a high-pass filter, low-pass filter and integrator in the system. The filters and integrator gain K are dependent on the frequency and amplitude of dithering, respectively. Therefore, it is chosen to investigate influence of w and a first, and tune the filters and integrator gain accordingly. The influence of parameters on performance is measured in two ways: Convergence speed and its ability to reject disturbances.

Section 8.2 shows the influence of dither frequency ω. The amplitude a will be discussed in Section 8.3. The phase alignment will be explained in Section 8.4. Finally, Section 8.5 concludes this chapter.

8.2. Dithering frequency ω

Here, the influence of dithering frequency on performance is measured. The convergence speed for various ω will be checked. Before doing so, however, the optimal feedback gain must be chosen. To do this, the algorithm is started at an initial position 2 µm away from the optimum. The algorithm will ensure the optimum will be found, with a certain aggressiveness determined by K. Figure 8.1 shows this response for ω = 100 Hz and various K's. The perturbation amplitude is kept constant, as is the High-Pass filter.

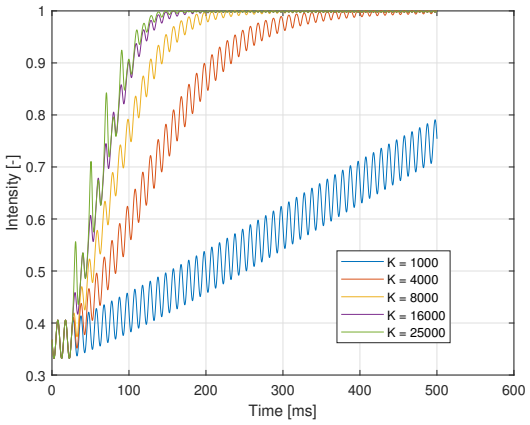

Figure 8.1: Step response for different K. ω = 100 Hz, a = 0.1 µm

It can be seen that increasing the feedback gain will lead to a faster response, up to a certain degree. Eventually, increasing feedback gain will only give more overshoot, resulting in poorer system performance. This

means there is a minimum settling time for each ω.

8.2.1. Convergence speed

The first condition ω is tested on is the time it takes to converge to its optimal value, starting from an initial suboptimal position. Figure 8.2 shows a system response for various ω. The HPF designed is $\frac{s}{s+\omega}$, as ω must not be attenuated for gradient estimation. The feedback gain was increased until the fastest response was found.

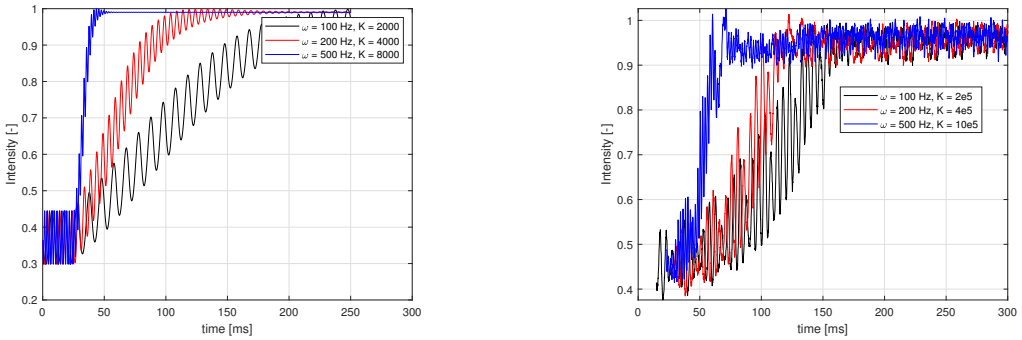

(a) Simulink model

(b) Experimental data

Figure 8.2: Convergence speed as simulated (a) and measured (b)

Note that the simulation and experiment use different values of K. This is because in the experiment, the digital to analog converter and FSM dynamics also have a certain gain which are not implemented in the simulation. For equal values of K, convergence speed will be the same regardless of ω. When the dithering frequency is increased, however, the gain can also be increased more before observing overshoot. This is due to the fact that a gradient is estimated every $\frac{1}{\omega}$ seconds. The faster the gradient is estimated, the faster the response of the system can be. The optimal K scales linearly with the frequency. Both Figure 8.2a and Figure 8.2b show that a higher ω leads to a faster optimal system response.

8.2.2. Disturbance rejection

The second condition the frequency analysis was subjected to is disturbance rejection. A sinusoidal disturbance of a certain frequency was imposed on the system and the performance was measured. This was done a number of times, for different disturance frequencies. Ideally, the system can fully reject these disturbances and keep tracking the optimum. It is expected, however, that as the disturbance frequency approaches the dithering frequency, the performance will drop due to the speed limits of the system. Figure 8.3 shows the performance over disturbance frequencies for three values of ω. The amplitude of the disturbance was 1 µm. The same K and a parameters were chosen as in the previous tests.

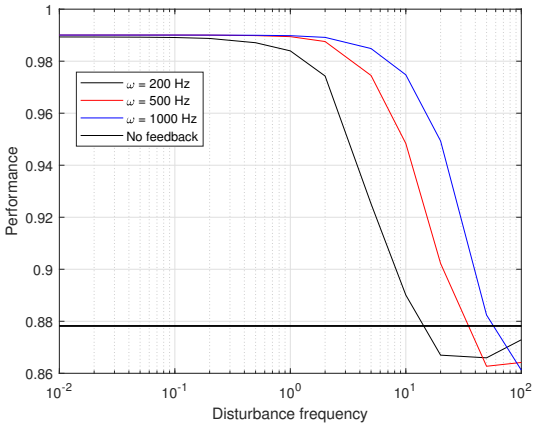

Figure 8.3: Disturbance rejection for various ω

A couple of things can be noted from this figure. The black line indicates the performance when the control algorithm is switched off. The average performance then is ≈ 88 %. With the ESC switched on, the performance increases to around 99 %. It does not completely converge to the optimum, but moves around it in a circle with radius a. Note also that for a certain frequency range the performance actually drops below the black line. This is because there is a certain delay in the feedback. As the disturbance frequency increases, this delay can decrease for certain frequencies. However, this test was merely to show the influence of the dithering frequency ω. In Chapter 9, more elaborate performance tests will be done.

Lastly, it can be noted that increasing the dithering frequency results in an increase of maximum disturbance frequency that can be properly rejected. Figure 8.4 shows the time response of a 200 Hz dithering frequency to a 1 µm disturbance of three frequencies.

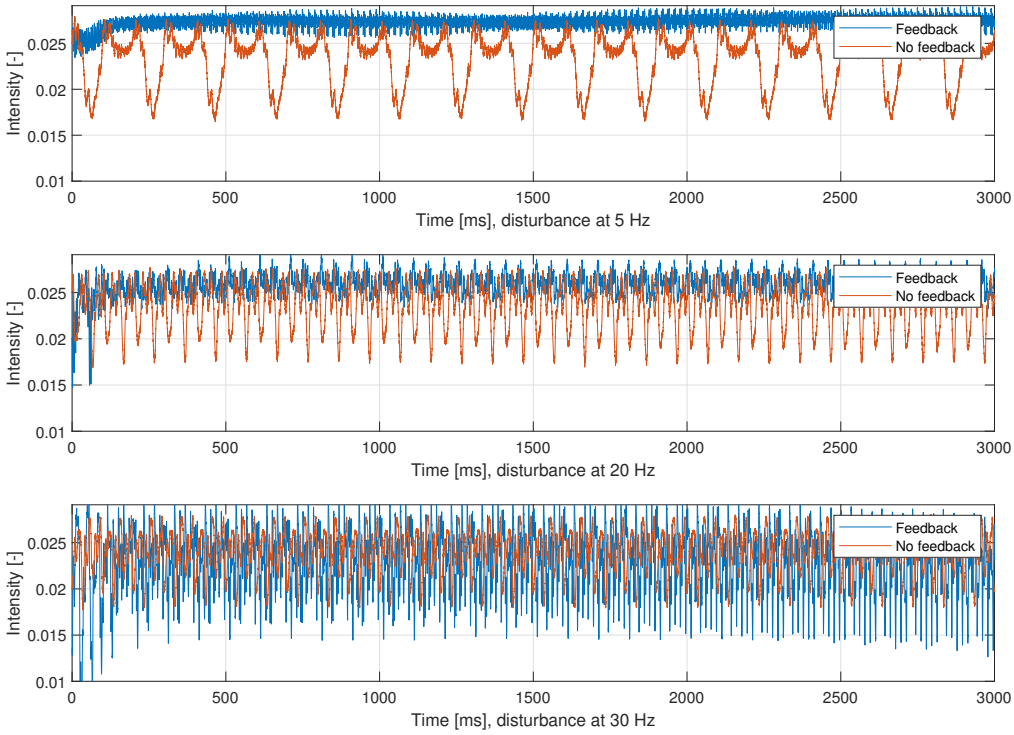

Figure 8.4: Intensity response to a disturbance of three different frequencies

The 5 Hz disturbance can be rejected properly, such that the intensity stays at its maximum. As the frequency increases, however, the algorithm is not fast enough to track the disturbance. Eventually this will lead to loss of performance, as the gradient can no longer be accurately estimated.

8.2.3. Frequency limits

The dithering frequency is limited in two ways. Firstly, the sampling frequency, F_s, of the system. An F_s that is not sufficiently high enough can result in effects as aliasing, where the sine wave cannot be measured back properly. This might result in system failure. This sampling frequency has a certain limit, depending on the RTC used and the computational power needed by the algorithm. For this setup, an F_s of 10 kHz was achievable. Secondly, the dithering frequency is limited by the dynamics of the FSM. The FSM behaves as a mass-spring-damper system, which reject higher frequencies. The characteristics of this FSM are measured by imposing a frequency-sweep on the system. The result is shown in Figure 8.5 and Figure 8.6.

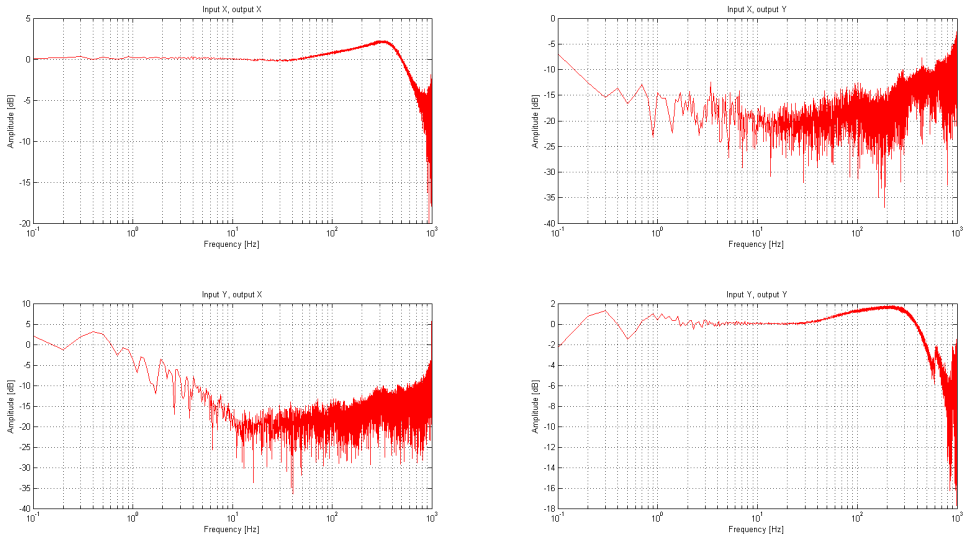

Figure 8.5: Magnitude plot of FSM response

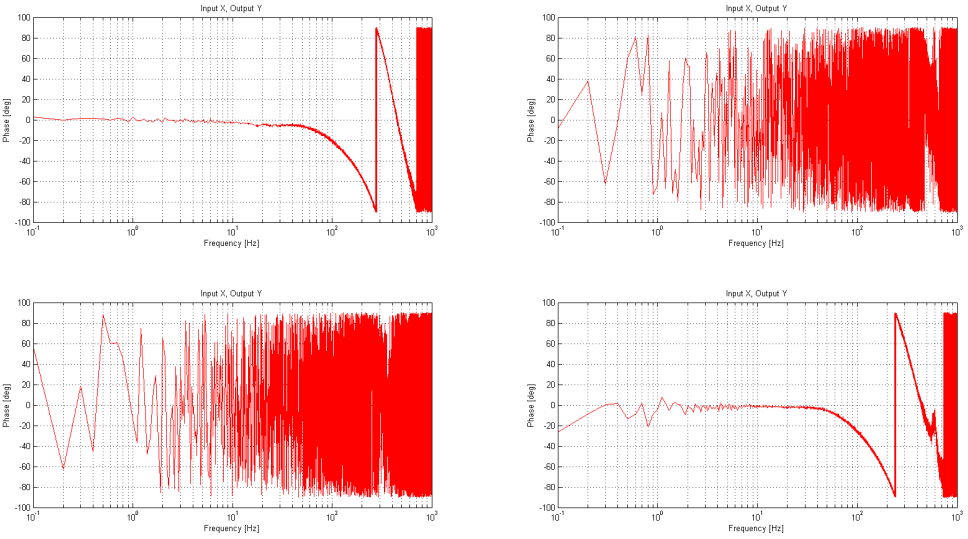

Figure 8.6: Phase plot of FSM response

When a input was applied on the horizontal (X) axis of the FSM, both the X-position and Y-position were measured. The top left and bottom right figures show the system response for the horizontal and vertical axis of the FSM, respectively. The cut-off frequency is approximately 500Hz for both axes. It can also be seen that applying an input to one axis does not yield large parasitic motion in the other axis. Choosing a excitation higher than 500 Hz increases the uncertainty of the response. This will make is more difficult to determine the spot position accurately.

In this setup, the FSM dynamics are limiting. The dithering frequency is chosen to be 500 Hz. With a sampling frequency of 10 kHz, this means a sine wave will consists of 20 samples.

8.2.4. HPF

After choosing the dithering frequency, the high-pass filter can be designed. As explained, this filter serves to remove the DC-gain of the intensity measurement, such that a gradient of the input-output mapping can be estimated. This filter must keep the 500 Hz component of the signal. In reality, however, this intensity signal will be subject to noise due to sensor dynamics, atmospheric tip/tilt, vibrations and thermal drift. Therefore, the real life system might need to attenuate higher frequency signals as well. An initial filter is shown in Equation (8.1).

$$HPF = \frac{s}{s+500} \tag{8.1}$$

Each system has its own sensor dynamics and noise. this means the design of this filter must be done based on the specific setup. The performance of the setup under the disturbances mentioned will be discussed in Chapter 9.

8.2.5. Conclusion

Increasing the dither frequency results in a faster system response, as long as the feedback gain K is increased in the same manner. The high-pass filter must can be designed accordingly. Increasing ω ensures higher frequency disturbances can be rejected. The FSM used in the experiment limits the maximum dithering frequency to 500 Hz. This is the value chosen for ω.

8.3. Dithering amplitude a

The next system parameter is the dithering amplitude a. This, together with the feedback gain K, determines the aggressiveness of the algorithm. The amplitude is subjected to the same two tests as the dithering frequency: Convergence speed and disturbance rejection. Equation (7.22) showed the estimation error, which indicates that a and K relate to each other in the following manner:

$$a \propto \frac{1}{K^2} \tag{8.2}$$

This means that if the amplitude is increased by a factor 2, the feedback gain must be decreased by a factor 4 to achieve the same performance. The amplitude is also subjected to tests of convergence speed and disturbance rejection. Both are elaborated upon below.

8.3.1. Convergence speed

Figure 8.7 shows the performance for two combinations of a and K.

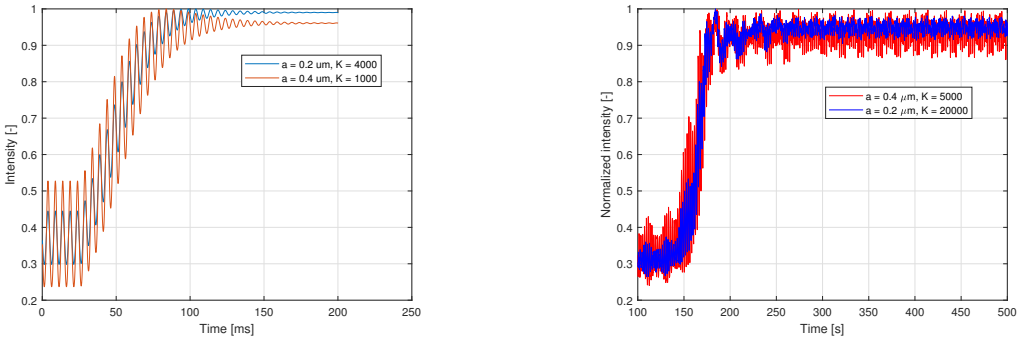

(a) Simulink model

(b) Experimental data

Figure 8.7: Convergence speed as simulated (a) and measured (b)

It can be seen that the settling time is the same, although the dithering amplitudes are different. This is a logical result, as the poles of Equation (7.22) lie at the same position for both combination of parameters. Note also that the maximum intensity it converges to is dependent on a: smaller amplitudes converge closer to the optimum. Now, there is a point where the relation shown in Equation (8.2) no longer holds. When a is made progressively smaller, a point comes where the system becomes slower, as can be seen in Figure 8.8.

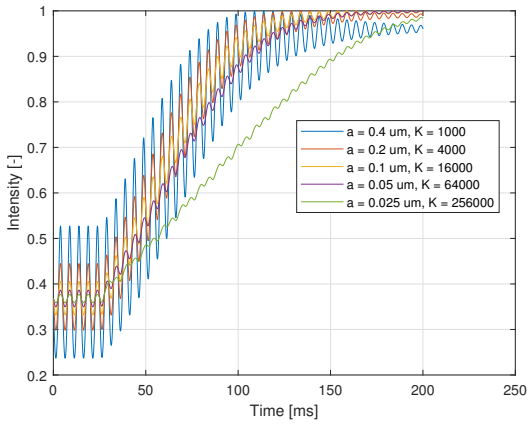

Figure 8.8: Influence of dithering amplitude

When the amplitude is decreased to 25 nm, the performance of the system drops. This can be explained by looking at the high-pass filtered signal. The signal for [a = 25 nm, K = 2.56e5] and [a = 100 nm, K = 1.6e4] are shown in Figure 8.9b.

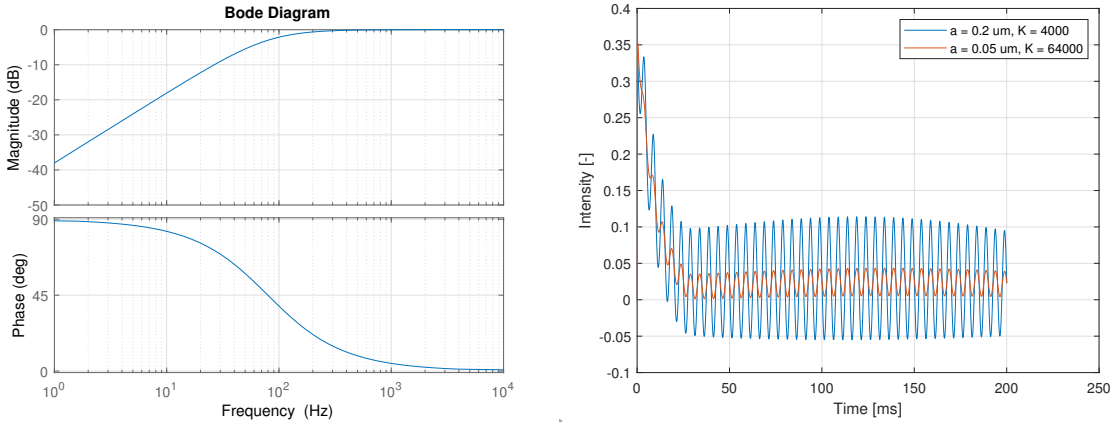

(a) Bode plot of initial high-pass filter

(b) High-pass filtered signal

Figure 8.9: System response for altered HPF

This high pass filter serves to remove the low frequency content of the intensity, such that the filtered signal oscillates around 0. However, if the amplitude of the 500 Hz component is so small, the lower frequency components start to play a role and the signal no longer oscillates around 0. This means the gradient can no longer be accurately determined. This can be solved by choosing a sharper filter. Figure 8.10b shows the High-pass filtered intensity for the same parameters, but with a high pass filter as shown in fig. 8.10a.

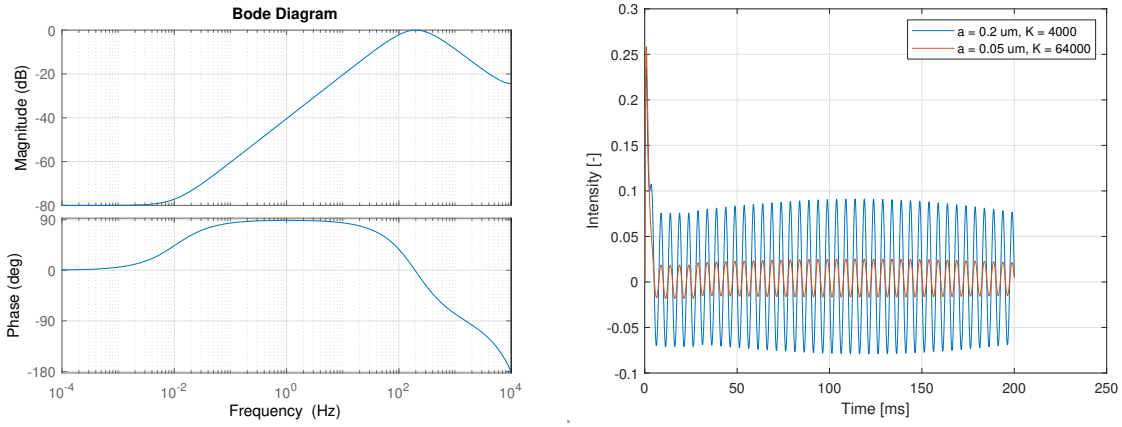

(a) Bode plot of High pass filter

(b) High-pass filtered signal

Figure 8.10: System response for altered HPF

Now, even for very small amplitudes, the gradient can still be properly measured. This means that theoretically, the amplitude can be infinitely small without losing system performance. As the convergence speed is the same and the maximum increases with smaller a, the amplitude should be as low as possible in terms of convergence speed.

8.3.2. Disturbance rejection

Figure 8.11 shows the disturbance rejection of the algorithm with ω = 500 Hz, for three values of a. Again, K is altered for optimal performance.

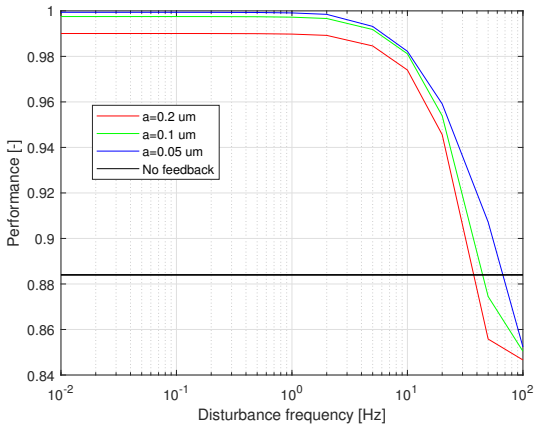

Figure 8.11: Disturbance rejection for different dithering amplitude

Again, the black line shows the average performance when the algorithm is switched off. As expected, smaller amplitudes give a higher maximum performance. As a grows larger, the performance drops for each frequency. This again results in a desire for an as small as possible a.

8.3.3. Limits of a

The amplitude is limited in two ways. Firstly, the resolution of the FSM. Too small inputs will not result in FSM movement. Secondly, the amount of noise in the system. When the amplitude grows smaller, noise becomes relatively larger up to a point where the sine wave is no longer visible. The FSM is controlled by a voltage input. The range of the FSM is [-1.5, +1.5]° and the voltage range [-10,10] V. Converted to µrad, an input of 0.04 V gives a rotation of 100 µrad. An angular movement results in twice the reflected movement, so 0.04 V is equal to a 10 µm spot deviation. Figure 8.12 shows the FSM sensor response for a 0.5 mV and 0 mV input.

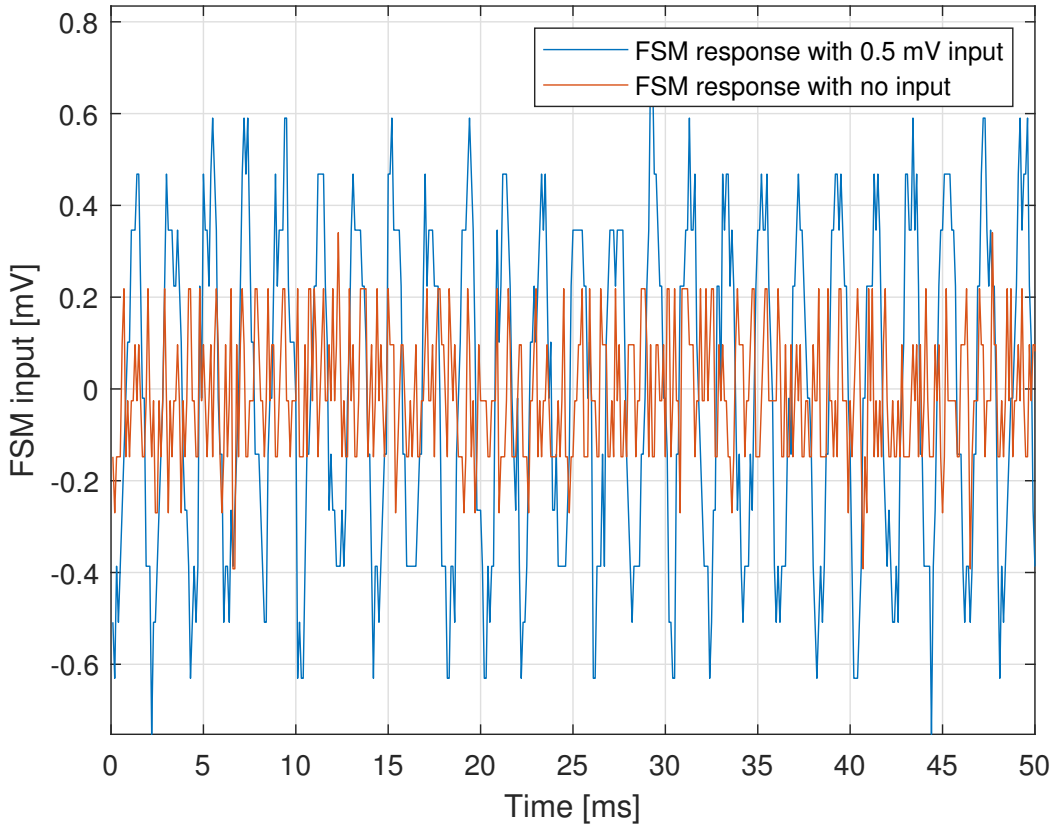

Figure 8.12: FSM system response. 0.5 mV corresponds to 1.25 µrad rotation.

Here, ω is 500 Hz. It can be seen that the amplitude of the present noise is approximately 0.1 mV. This does mean that the 0.5 mV can still be distinguished by the FSM sensor. This value corresponds to a 1.5 µrad rotation. This roughly corresponds to the FSM resolution specified by the manufacturer (which was <1.2 µrad). Translates into spot deviation, this will be 0.13 µm.

Figure 8.13 shows the intensity response for three amplitudes. Remember that the feedback gain is adjusted each time the amplitude is changed.

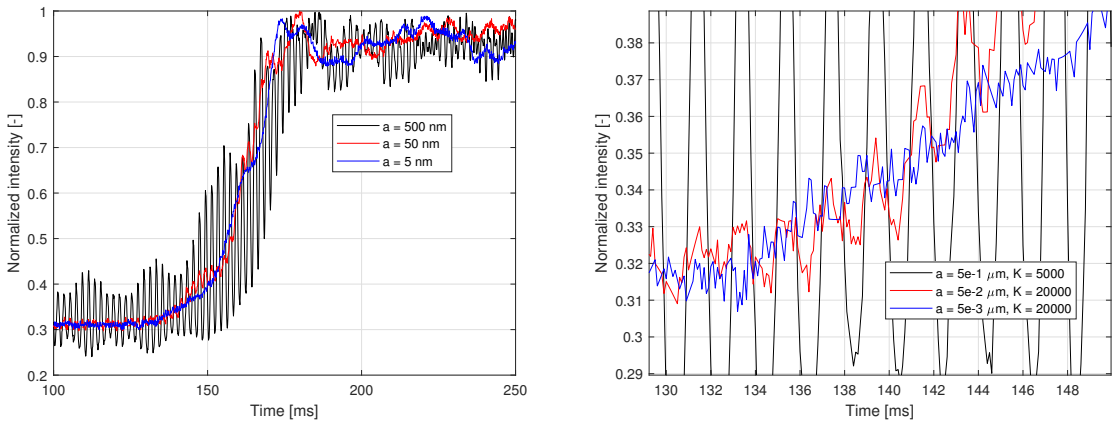

(a) Total view

(b) Zoomed view

Figure 8.13: Convergence speed for three amplitudes a. ω = 500 Hz

The convergence speed stays the same as we keep decreasing a. Note that the FSM can no longer measure the blue and red signal, but the optimal position can still be found. This means the the resolution of the FSM is not limiting. The blue line shows an amplitude plot of 5 nm. The dithering is almost no longer visible due to noise, but the gradient can still be found. This is because the high-pass filter greatly attenuates frequencies other than 500 Hz. In disturbance environments, however, the amount of noise will be increased. Furthermore, an a of 0.1 already converges to an intensity that is 99.7% of it's maximum value. It therefore does improve much to decrease the amplitude more than this, and the risk of increased noise is always present. Therefore, a dithering amplitude of 0.1 μm is chosen.

8.3.4. Conclusion

Smaller amplitudes lead to a convergence closer to the optimum, as well as better performance at disturbance rejection. As K is inversely proportional to the square of the amplitude, the feedback gain can be chosen accordingly. The amplitude is eventually limited by noise due to various disturbances, which render it more difficult to determine the gradient information. An amplitude of 0.1 μm already ensures the algorithm converges to an intensity that is 99.7% of the maximum achievable intensity. This means decreasing the amplitude even further does not improve the system much. The same argument holds for disturbance rejection. Therefore, the dithering amplitude is chosen to be 0.1 μm.

8.4. Phase alignment

The phase delay at 500 Hz due to the high-pass filter is 0 by design, as it is an inverted notch with its peak at 500 Hz. The phase delay due to the FSM is estimated to be ≈ 9°. The input was given the same delay and matched with the high-pass filtered output. This is shown in Figure 8.14. This shows the input, delayed. The y-position was given an offset of positive 2 μm. The parameters are the same as used for the intensity plot shown in fig. 8.7b.

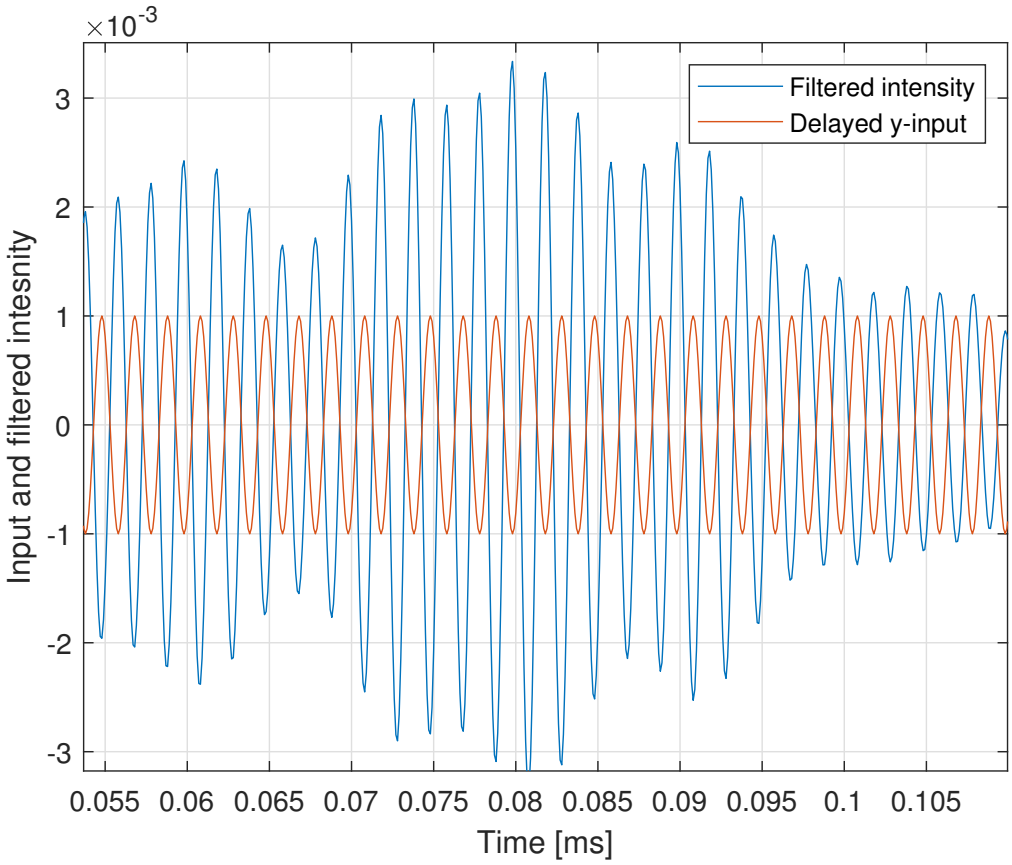

Figure 8.14: Input and output signal. Note that the phase difference is exactly 180°

Note that this delay is not dependent on time, as both FSM and high-pass filter have a constant delay when ω is constant. As the deviation in y-direction was positive, we expect a negative gradient. The product of the two sine waves shown is indeed purely negative, which means the phase delay was correctly estimated. The input for both x and y was delayed by 8 samples or 0.8 ms to achieve this performance.

8.5. Conclusion

The four parameters that can be tuned are the dithering frequency ω, the dithering amplitude a, the high-pass filter and the feedback gain K. This chapter analysed the influence of each of them on system performance. This lead to the choice of parameters shown in Table 8.1. Furthermore, the phase between input and output signal was estimated by analysing the system dynamics. For this system, the input must be delayed by 0.8 ms or 8 samples for optimal performance.

Parameter	Value	Description
ω	500 Hz	Dithering frequency
HPF	$\frac{s^2+c*s+500^2}{10^4(s^2+c*s+500^2)}$	High-pass filter
a	0.1 µm	Dithering amplitude
K	1.6e3	Feedback gain

Table 8.1: Optimal control parameters

9

Control performance on experimental setup

Now that the optimal system parameters are known for this setup, the performance of the algorithm under different disturbances will be analysed. section 9.1 shows the derivation of a Power Spectral Density (PSD) of the setup. Using this, Section 9.2 discusses the influence of atmospheric tip/tilt. The effects of satellite microvibrations are discussed in Section 9.3. Section 9.4 shows the performance when the fiber coupling system is subjected to thermal drift. Section 9.6 concludes this chapter.

9.1. Derivation of system Power Spectral Density

The effectiveness of disturbance rejection can best be expressed by means of a Power Spectral Density (PSD). Disturbances such as vibrations and atmospheric tip/tilt are generally expressed using PSD's.

An estimate of the system PSD is derived by implementing white noise on the system and measuring the PSD of the control signal. The system PSD is then calculated by Equation (9.1)

$$PSD_{system} = \frac{PSD_{Output}}{PSD_{Input}} \tag{9.1}$$

Figure 9.1 shows the spot deviation due to a disturbance signal (black), the feedback due to the ESC algorithm (red) and the total spot position (blue) over a timespan of 500 ms.

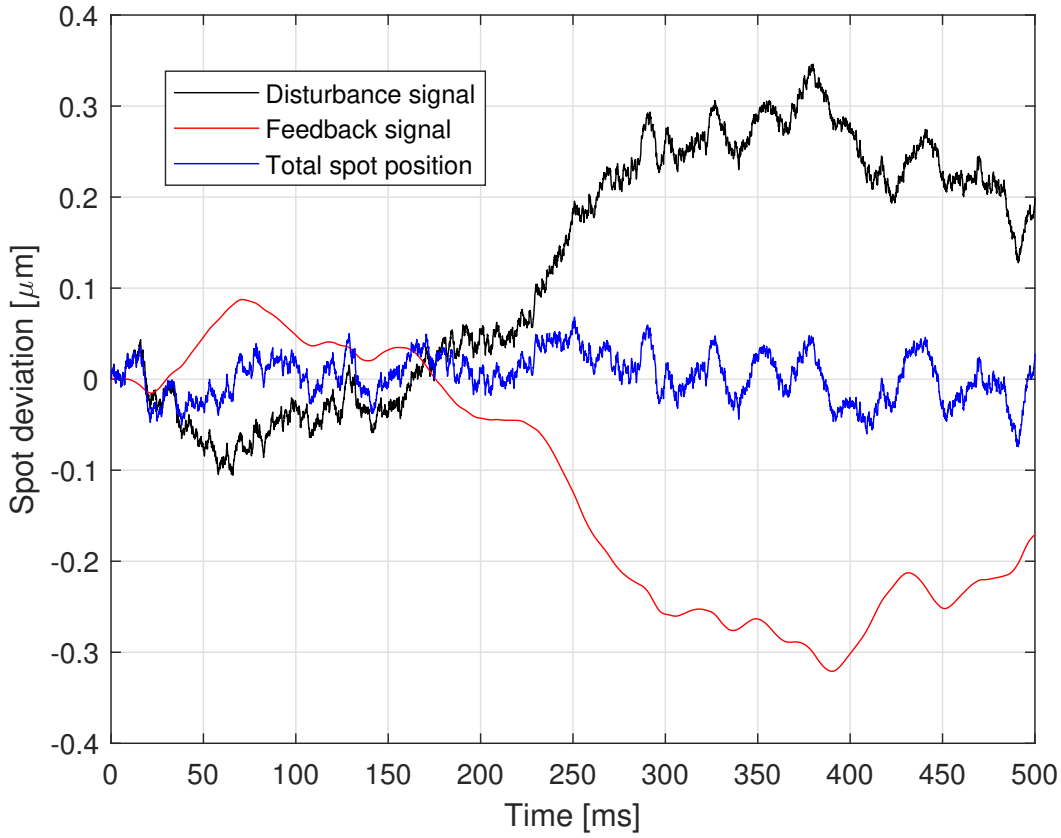

Figure 9.1: Time domain signal of noise, feedback and control position

Here, the spot position is the sum of the disturbance and the feedback signal. It can be seen that when the spot changes due to the disturbance, the feedback keeps the spot position approximately at its 0 position. Higher order frequencies, however, are more difficult for the algorithm to reject. Figure 9.2 shows the PSD of the disturbance signal (black) and the spot position (blue).

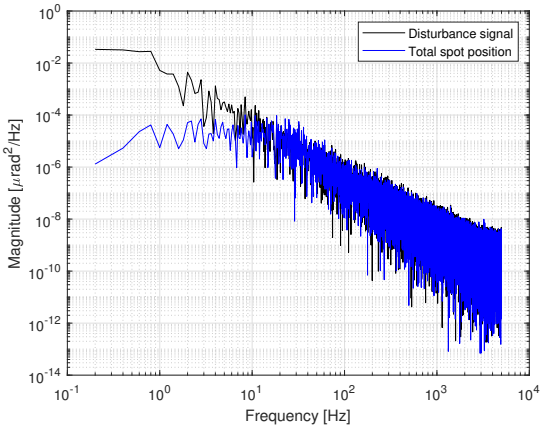

Figure 9.2: PSD of disturbance and spot position

It can be seen that most low-frequency signal content is attenuated. The system PSD can now be estimated using Equation (9.1). Figure 9.3 shows the simulated PSD content, as well as an approximation for a dithering frequency of 500 Hz.

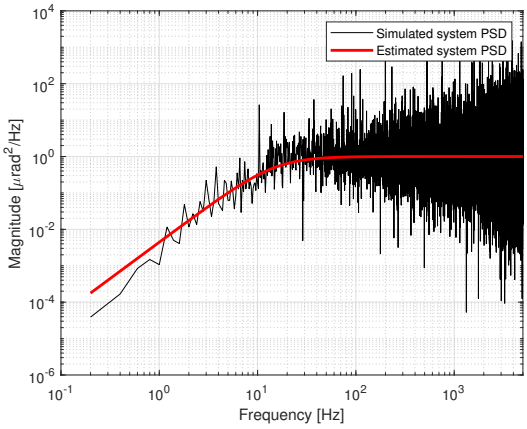

Figure 9.3: PSD of disturbance and spot position

It shows that low frequency disturbances are attenuated. At around 15 Hz, the signals are no longer properly rejected. Higher frequency components fully remain in the signal and will impact performance. The estimated PSD is shown in Equation (9.2).

$$PSD_{System} = \left(\frac{s}{s + \frac{\omega}{30}}\right)^2 \tag{9.2}$$

Here, the ω is the dithering frequency. For various dithering frequencies, coupling loss due to atmospheric turbulence and vibrations is analysed. The Remainder of Coupling Efficiency () is shown for a range of dithering frequencies in Figure 9.4.

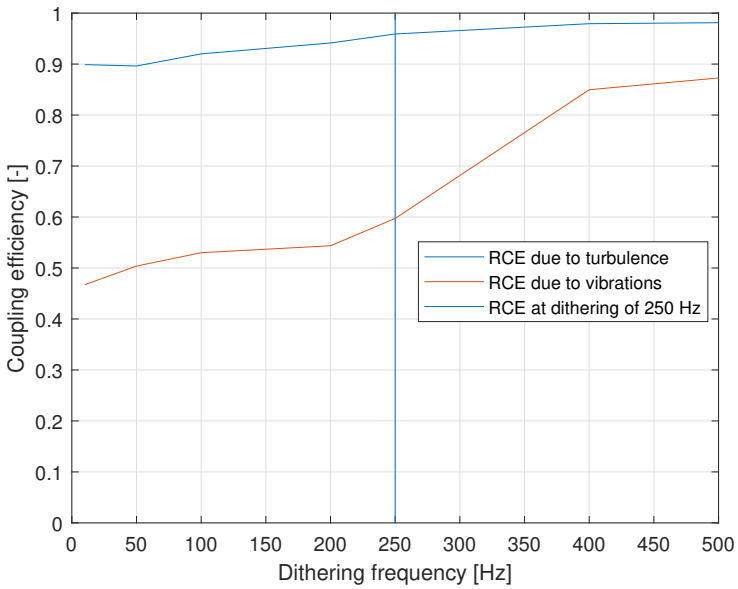

Figure 9.4: Remainder of coupling efficiency due to atmospheric turbulence (blue) and satellite microvibrations (red). At 250 Hz, these values are 0.96 and 0.59 respectively.

For a set of dithering frequencies, the algorithm was run for 120 seconds to see the average coupling efficiency. It was determined in Table 4.2 that the combined effects of turbulence and vibrations must not result in a mamimum RCE of 0.53. By taking the product of these two losses, it can be found that a dithering frequency of 250 Hz results in a Remainder of Coupling efficiency of .57. Therefore, the minimal dithering frequency of the algorithm, for this application, is 250 Hz. However, this can be improved by increasing the dithering

frequency. How this requirement is derived, and what the performance can be of the system, is shown in Section 9.2 and Section 9.3.

9.2. Atmospheric tip/tilt

This chapter shows the performance tests that were done on the optical setup. Atmospheric tip/tilt is mainly relevant for the downlink. For an uplink, propagation after atmospheric turbulence is so large, that the turbulence will not be measurable in the satellite. Although this thesis focuses on fiber coupling in a satellite, the algorithms can be used for receiving links from a satellite as well. Therefore, the performance is investigated for this disturbance. Figure 9.5 shows a PSD plot of a general tiptilt situation.

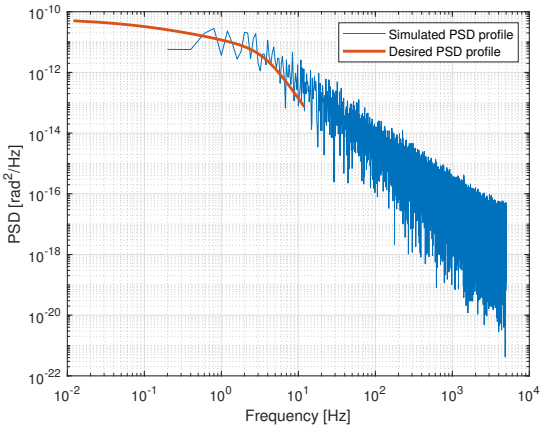

Figure 9.5: PSD of atmospheric turbulence

The approximation of the tip/tilt disturbance is shown in red. In blue, the PSD of a simulated time signal that is to match this approximation is shown. This is the tip/tilt arriving at the FSM fiber coupler. This tip/tilt will result in a defocus due to the focusing mirror with a focal length of 47 mm. This means the signal must be converted from rad to µm. Figure 9.6 shows the PSD of the spot deviation due to atmospheric tip/tilt.

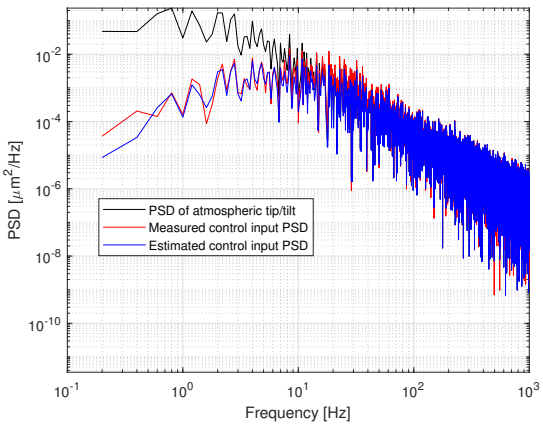

Figure 9.6: PSD of atmospheric turbulence

In black, the PSD in $\mu m^2/Hz$ is shown. In blue, the estimation of remaining turbulence. This is constructed by multiplying the PSD of atmospheric turbulence by the system PSD constructed in Section 9.1. As can be seen, the simulation coincides well with the estimation. Especially low frequency components are attenuated, such that the position stays closer to the optimum. Figure 9.7 shows the intensity over time for both with and without ESC turned on.

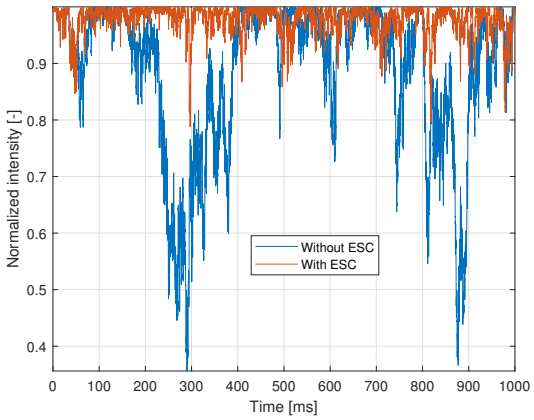

Figure 9.7: Simulated performance plot over time

It can be seen that the algorithm ensures the spot stays closer to the optimum. The average intensity value for no feedback is 88%, with feedback 98%. The requirement was that atmospheric tip/tilt would amount to at most 10% efficiency loss, which is met. In fact, the efficiency loss is only two percent, which means the performance is better than expected.

9.3. Vibration analysis

The same performance tests will be shown here on vibrations. Figure 9.8 shows the ESA standard for satellite microvibrations.

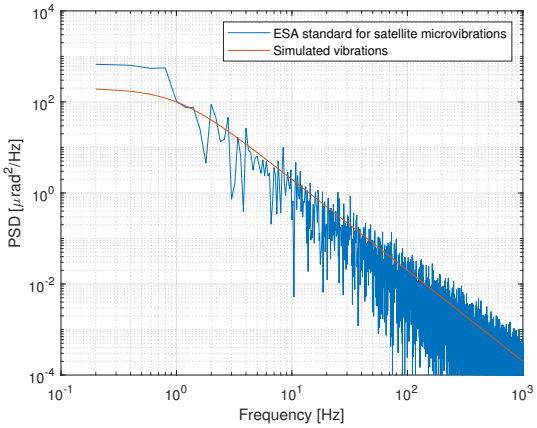

Figure 9.8: PSD for satellite microvibrations

These vibrations will rotate the entire satellite. The actual tip/tilt on hte fiber coupling subsystem is determined by the angular magnification, i.e. the ratio between entrance aperture and fiber coupling aperture. An angular magnification of 4 is chosen. Again, the spot deviation can be calculated by taking the product of the tip/tilt with the focal length of the mirror. This gives the following spot deviation plot:

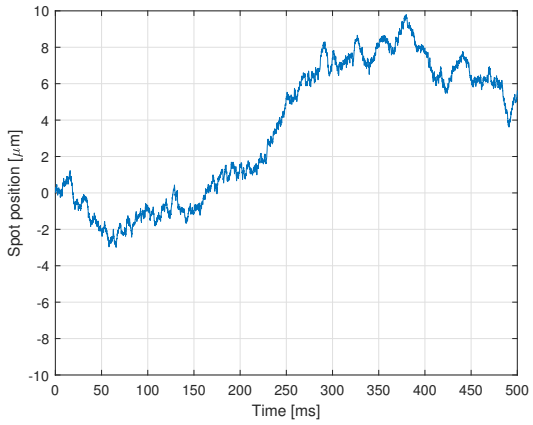

Figure 9.9: Spot deviation over time

The spot position can deviate up to 10 µm due to satellite microvibrations. This means that without feedback control, the performance will drop to 0. Figure 9.10 shows the PSD for spot deviation when the ESC algorithm is turned on.

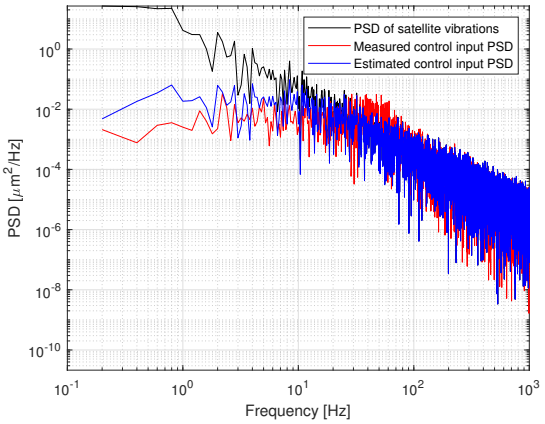

Figure 9.10: PSD for vibrations with ESC turned on

Again, it can be seen that the estimation fits quite well with the measured data. Figure 9.11 shows an intensity plot over time, both with and without the ESC algorithm.

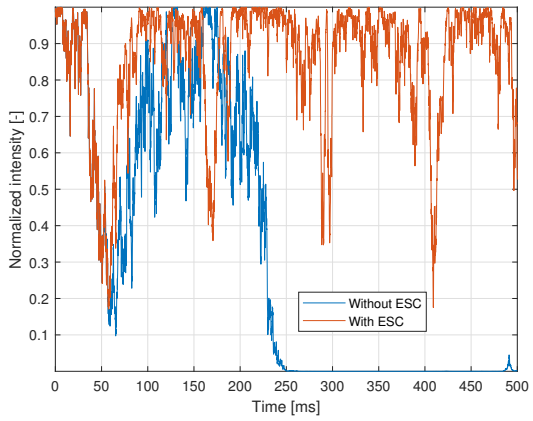

Figure 9.11: Intensity plot over time

The performance is a lot worse than for atmospheric tip/tilt. This is because the amplitude of vibrations are a lot larger. It can be seen that the control ensures that the spot stays around the optimum. The mean intensity over 20 seconds is 84% with ESC, 39% without ESC. The requirement on atmospheric tip/tilt was 0.7, which is met. Again, the performance can be better than was required. However, it can be seen that the performance sometimes shows a large dip, which will results in a larger Bit Error Rate. So while the average efficiency is sufficient, these dips might still result in poor system performance. A way to mitigate this, is by using an FSM that has a bandwidth higher than 500 Hz. In that case, performance will be more constant, as is shown in Figure 9.7. Furthermore, the average coupling efficiency increases even further. TNO has developed an FSM which has a bandwidth of >1000 Hz. It is definitely a recommendation to see how well this FSM would reject disturbances and thereby how much the fiber coupling efficiency can be improved further.

9.4. Thermal drift analysis

An optical design that expands or contracts homogeneously should not result in loss of performance. In fact, it is usual in the optical design of a satellite to ensure it is thermally centered, to negate exactly these effects. However, in many on earth-tests, the setups are subject to thermal drift due to the varying temperature of the room. The Extremum Seeking Control can be applied in these situations, to keep track of the optimum while thermal drift takes place. The period of these changes is in the order of minutes. When a sinusoidal perturbation of 0.01 Hz with amplitude 10 μm is applied, the performance would drop to 0 %. With Extremum Seeking Control, however, the normalized performance has a mean of 99.7%. This means Extremum Seeking Control is especially powerful when low frequency perturbations are added to the system, as was expected.

9.5. Overall system performance

All requirements imposed on the system can be met. Table 9.1 shows the required Remainder of Coupling Efficiency due to various factors, and the expected performance.

Table 9.1: Coupling loss budget [20]

Contributor	Initial error budget	RCE current	Expected Performance	RCE new
Light going to quadcel		-		-
Theoretical efficiency		0.817		0.817
Fresnell losses		0.96		0.96
Fiber decenter	2 μm (stability + alignment)	-		-
Fiber tip/tilt	1.41°	0.946		0.97
Fiber defocus	20 μm	0.984		0.984
WFE	100 nm RMS	0.837		0.837
Atmospheric tip/tilt		0.9		0.98
Satellite microvibrations		0.7		0.84
Dithering amplitude a		0.98		0.997
Total		0.352		0.501
Requirement		0.35		0.35
margin		0.5 %		43.2%

The tip/tilt and defocus requirements are met in terms of manufacturing, due to alignment with shimming of the z-axis. The tip/tilt is in fact expected to have an RCE of 0.97. The Extremum Seeking control, in its current optimal performance, the requirements are met and the average performance is improved. The dithering amplitude could be a lot smaller, resulting in a higher RCE. The overall average performance is expected to increase by 40%. However, satellite vibrations will result in a largely fluctuating fiber coupling efficiency. It is important to find out the impact of this on link establishment.

9.6. Conclusion

The optimal Extremum Seeking control parameters can ensure the requirements imposed on the system can be met. Main disturbances are atmospheric tip/tilt, satellite microvibrations and thermal drift. The Remainder of Coupling Efficiency due to these factors is 0.98, 0.84 and 1, respectively. As they are higher than required, the average coupling efficiency is expected to improve by 40%.

10

Conclusion

The objective of this report was to investigate how fiber coupling can be improved in optical communication systems. This was achieved by analyzing current systems and their drawbacks.

Free Space Optical (FSO) communication will considerably increase data capacity with respect to more mature Radio Frequency technologies. Additionally, FSO links are more secure, require no spectrum licensing and can be used were optical fibers cannot be used. Current fiber coupling systems are effective in establishing robust, high-capacity optical links between satellites and ground stations. They accomplish this by sensors which accurately determine beam position and correctly guide the beam into an optical fiber. However, these sensors require a part of the beam intensity to function. Additionally, there will always be internal drift and vibrations to some degree, due to imperfect design or alignment.

After considering different approaches in improving fiber coupling efficiency, sensorless fiber coupling is deemed the most promising approach. It will substantially relax alignment and design tolerances, as the fiber position is no longer a factor in proper system functioning. Removing the beamsplitter and position sensor also reduces the complexity of the system and increases intensity that reaches the fiber.

A design has been made that relies on Extremum Seeking Control for tracking the fiber position. All requirements for this design can be met. A model of the system is built to verify this and a breadboard experiment has been done. The results show that Extremum Seeking Control can achieve fiber coupling, while attenuating disturbances such as atmospheric tip/tilt, satellite vibrations and fiber drift due to thermal effects.

It is shown that the average fiber coupling efficiency can be improved with respect to a comparable fiber coupler at TNO by approximately 40%. However, this average performance does not show the fluctuations due to high frequency satellite vibrations. Short drops in performance will substantially increase the Bit Error Rate. The impact of this on link establishment is not analysed, as the setup only focused on intensity measurement rather than data transfer.

Reccomendations

A first recommendation is to do a more elaborate research on the Bit Error Rate, and whether this system would meet performance requirements of link Establishment in general.
Secondly, by increasing the control bandwidth, the system performance would increase even more. TNO has an FSM available with a bandwidth of >1000 Hz. It is recommended to repeat the breadboard experiment with this FSM, to see how much performance can be increased further.

A

Appendix A: Figures of optical design

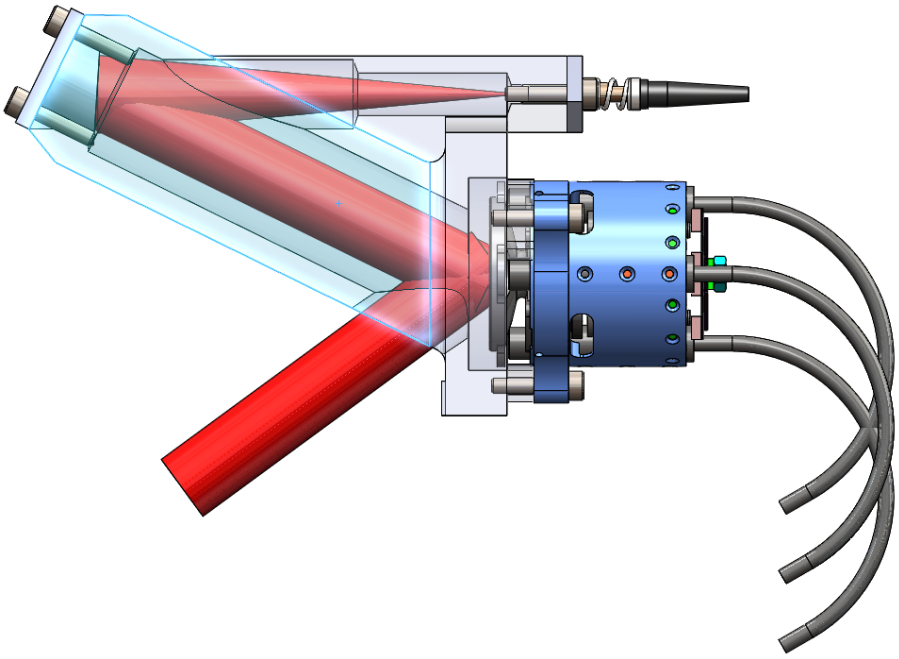

Figure A.1: Side view (transparent housing

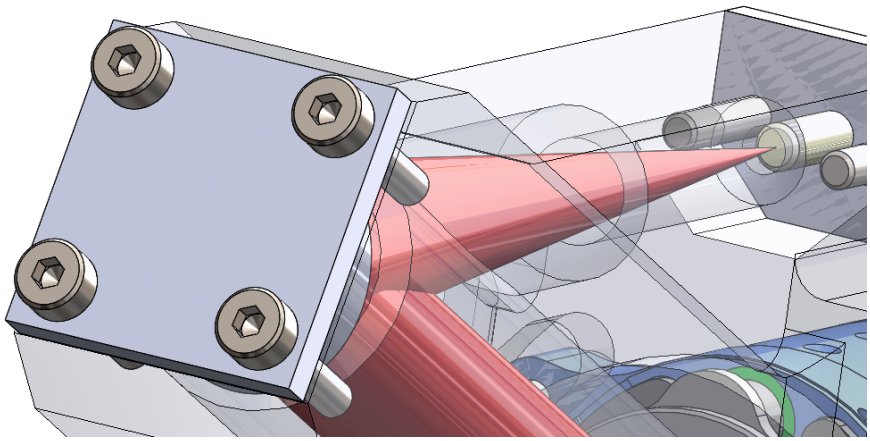

Figure A.2: Parabolic mirror

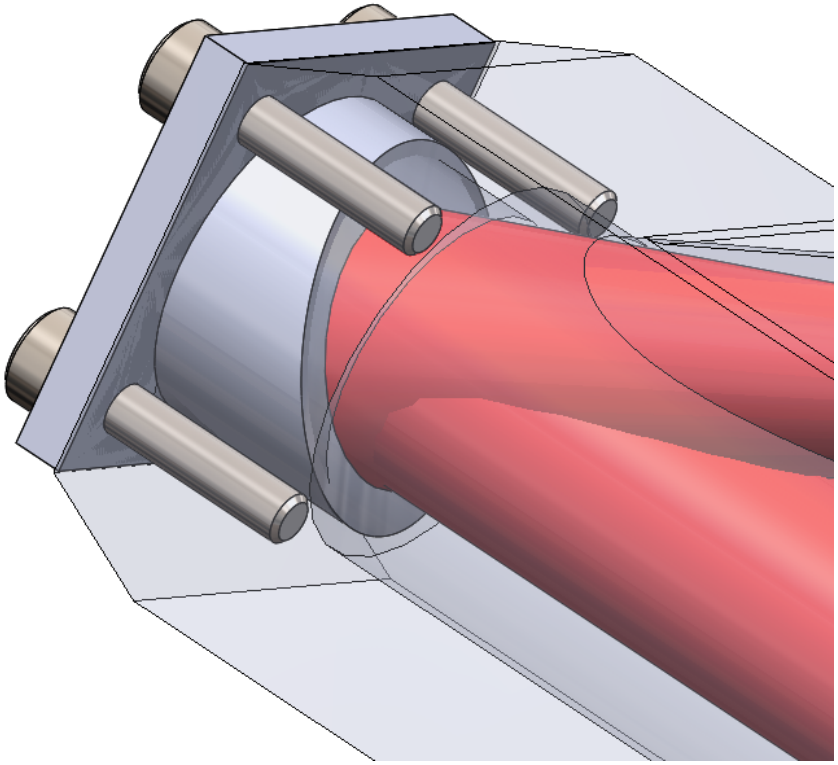

Figure A.3: Parabolic mirror

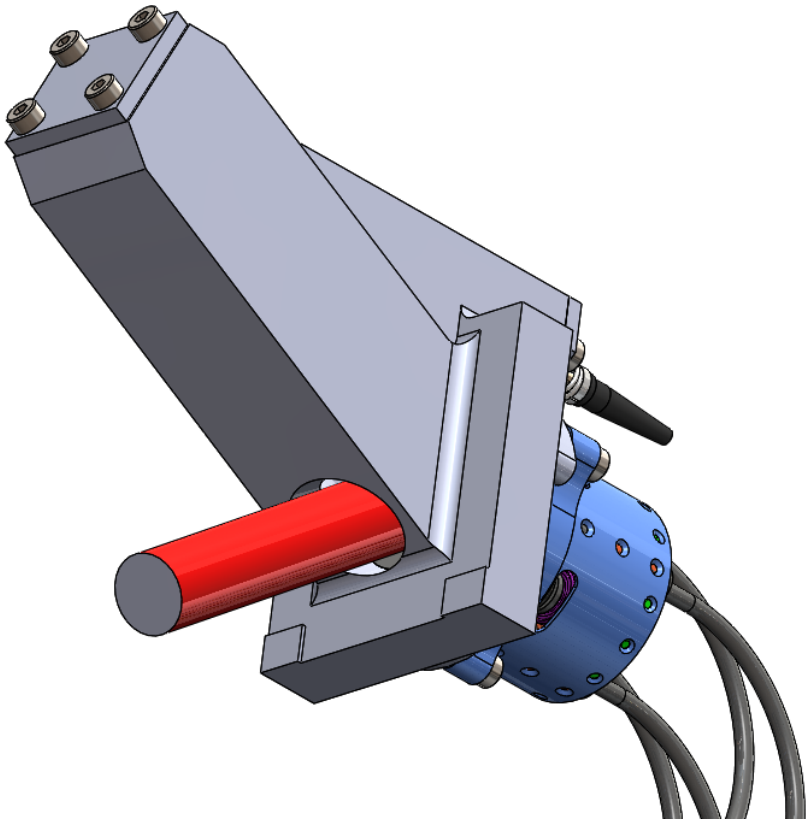

Figure A.4: Incoming laser beam

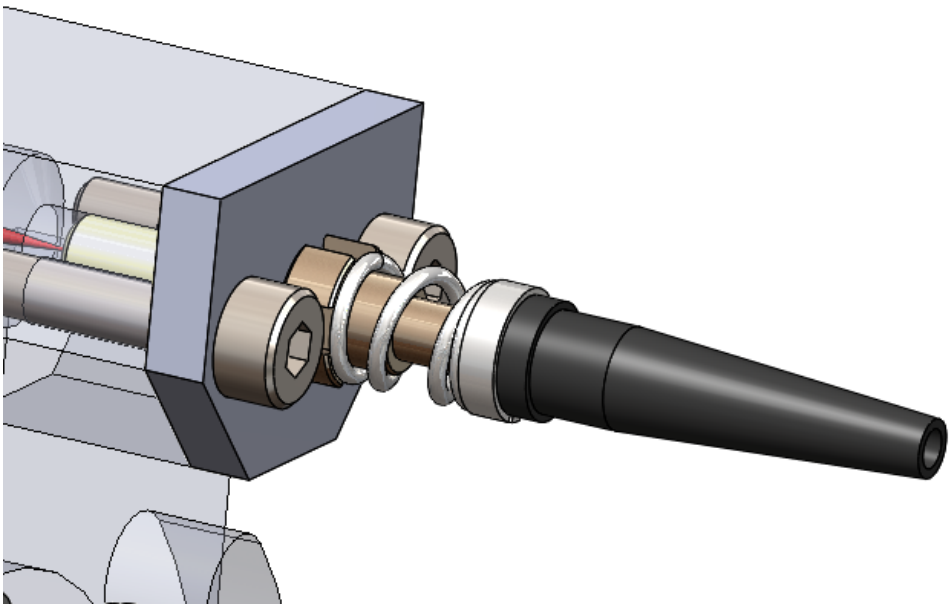

Figure A.5: Fiber connection

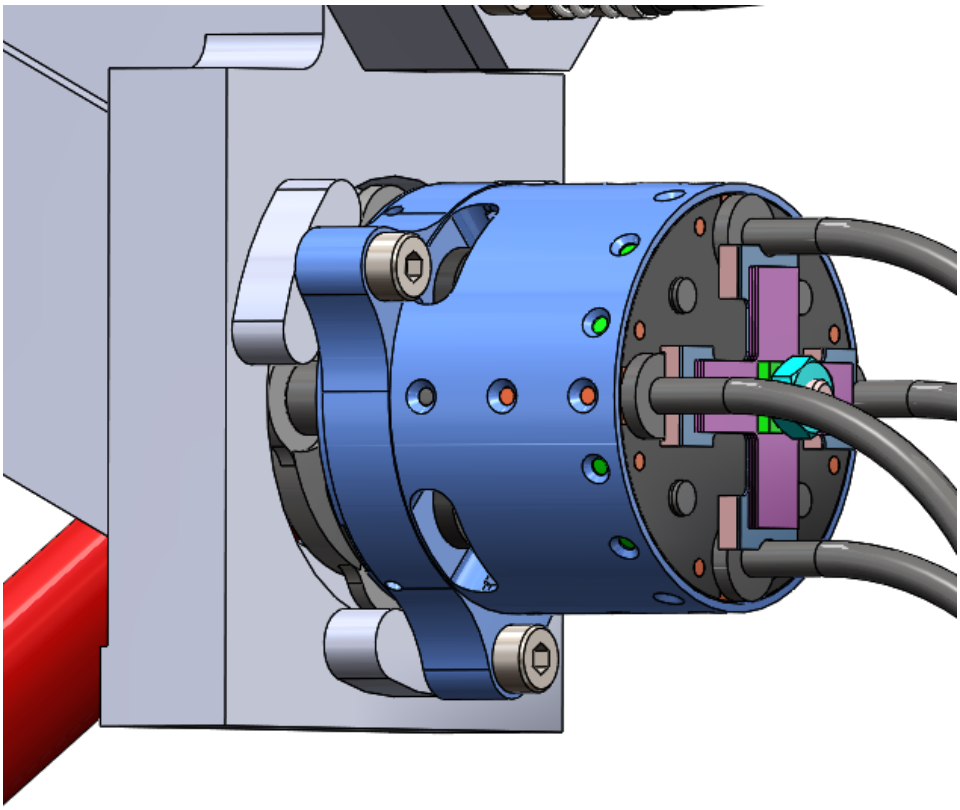

Figure A.6: FSM connection

Bibliography

[1] Introduction to fiber optics_proved.

[2] (Prentice-Hall International Series in Optoelectronics) John M. Senior, P. J. Dean-Optical Fiber Communications-Longman Higher Education (1985).

[3] *Space Mission Analysis and Design*. 1991. ISBN 978-0-7923-0971-0. doi: 10.1007/978-94-011-3794-2.

[4] The Zettabyte Era: Trends and Analysis. Technical report, 2017.

[5] Issue 1.0 Space Systems Engineering. Technical report, 2018.

[6] Larry C. Andrews and Ronald L. Phillips. *Laser Beam Propagation through Random Media*. 2005. ISBN 9780819459480. doi: 10.1117/3.626196.

[7] Steven L. Brunton, Xing Fu, and J. Nathan Kutz. Self-Tuning Fiber Lasers. *IEEE Journal of Selected Topics in Quantum Electronics*, 2014. ISSN 21910359. doi: 10.1109/JSTQE.2014.2336538.

[8] M. Guelman, A. Kogan, A. Kazarian, A. Livne, M. Orenstein, H. Michalik, and S. Arnon. Acquisition and pointing control for inter-satellite laser communications. *IEEE Transactions on Aerospace and Electronic Systems*, 2004. ISSN 00189251. doi: 10.1109/TAES.2004.1386877.

[9] Nasa / Amber Jacobson. NASA's first dedicated laser communication in space, the Lunar Laser Communications Demonstration (LLCD) Mission on NASA's LADEE spacecraft in 2013, sent data across 400,000 km at a rate of 622 Mb/s. Technical report, 2016.

[10] Juan C. Juarez, Anurag Dwivedi, A. Roger Hammons, Steven D. Jones, Vijitha Weerackody, and Robert A. Nichols. Free-space optical communications for next-generation military networks. *IEEE Communications Magazine*, 2006. ISSN 01636804. doi: 10.1109/MCOM.2006.248164.

[11] G L Knestrick, T H Cosden, and J A Curcio. Atmospheric Scattering Coefficients in the Visible and Infrared Regions. Technical report.

[12] Miroslav Krstić and Hsin Hsiung Wang. Stability of extremum seeking feedback for general nonlinear dynamic systems. *Automatica*, 2000. ISSN 00051098. doi: 10.1016/S0005-1098(99)00183-1.

[13] F. Nadeem, T. Javornik, E. Leitgeb, V. Kvicera, and G. Kandus. Continental fog attenuation empirical relationship from measured visibility data. *Radioengineering*, 2010. ISSN 12102512.

[14] NASA. North Africa and the Mediterranean Sea, 2018. URL `https://www.nasa.gov/sites/default/files/thumbnails/image/iss057e000244.jpg`.

[15] R C Olsen. *Remote Sensing from Air and Space*. 2007. ISBN 9780819462350. URL `www.spie.org`.

[16] Rudolf Saathof, Will Crowcombe, Stefan Kuiper, Federico Pettazzi, Amir Vosteen, Nick Van Der Valk, Niel Truyens, Remco Breeje, and Ivan Ferrario. TNO optical communications space terminals - Current projects and future plans. In *2017 IEEE International Conference on Space Optical Systems and Applications, ICSOS 2017*, 2018. ISBN 9781509065110. doi: 10.1109/ICSOS.2017.8357401.

[17] Rudolf Saathof, Remco Den Breeje, Wimar Klop, Stefan Kuiper, Niek Doelman, Federico Pettazzi, Amir Vosteen, Niel Truyens, Will Crowcombe, Jet Human, Ivan Ferrario, Ramon Mata Calvo, Juraj Poliak, Ricardo Barrios, Dirk Giggenbach, Christian Fuchs, and Sandro Scalise. Optical technologies for terabit/s-throughput feeder link. In *2017 IEEE International Conference on Space Optical Systems and Applications, ICSOS 2017*, 2018. ISBN 9781509065110. doi: 10.1109/ICSOS.2017.8357221.

[18] Morio Toyoshima. Trends in satellite communications and the role of optical free-space communications [Invited]. Technical report, 2005.

[19] Morio Toyoshima. In-orbit measurements of spacecraft microvibrations for satellite laser communication links. *Optical Engineering*, 2010. ISSN 0091-3286. doi: 10.1117/1.3482165.

[20] Frank Verhofstad. Template Space and Science project documenten. Technical report, 2018.

[21] R. E. Wagner and W. J. Tomlinson. Coupling efficiency of optics in single-mode fiber components. *Applied Optics*, 1982. ISSN 0003-6935. doi: 10.1364/AO.21.002671.

[22] W Dan Williams, Michael Collins, Don M Boroson, James Lesh, Abihijit Biswas, Richard Orr, Leonard Schuchman, and O Scott Sands. RF and Optical Communications: A Comparison of High Data Rate Returns From Deep Space in the 2020 Timeframe. Technical report, 2007. URL `http://www.sti.nasa.gov`.